The influence of natural variability on extreme monsoons in Pakistan

Moetasim Ashfaq[1], Nathaniel Johnson[2], Fred Kucharski[3], Noah S. Diffenbaugh[4], Muhammad Adnan Abid[3], Matthew F. Horan[5], Deepti Singh[6], Salil Mahajan[1], Subimal Ghosh[7], Auroop R. Ganguly[8], Katherine J. Evans[1], and Shafiqul Islam[9]

[1]Computational Sciences and Engineering Division (CSED), Oak Ridge National Laboratory, Oak Ridge, TN, USA
[2]National Oceanic and Atmospheric Administration/Geophysical Fluid Dynamics Laboratory, Princeton, NJ, USA
[3]Earth System Physics, Abdus Salam International Centre for Theoretical Physics, Trieste, Italy
[4]Doerr School of Sustainability, Stanford University, Stanford, CA, USA
[5]Bredesen Center, University of Tennessee, Knoxville, TN, USA
[6]School of the Environment, Washington State University, Vancouver, WA, USA
[7]Department of Civil Engineering, Indian Institute of Technology Bombay, Mumbai, India
[8]Sustainability and Data Sciences Laboratory, Civil and Environmental Engineering, Northeastern University, Boston, MA, USA
[9]Department of Civil and Environmental Engineering, The Fletcher School of Law and Diplomacy, Tufts University, Medford, MA, USA.

March 26, 2023

Abstract

The monsoons in Pakistan have been exceptionally harsh in recent decades, resulting in extraordinary drought conditions and record flooding events. The changing frequency of extreme events is widely attributed to climate change. However, given this region's long history of floods and droughts, the role of natural climate variability cannot be rejected without a careful diagnosis. Here, we examine how oceanic and atmospheric variability has contributed to unusual precipitation distributions in West South Asia. Variations in sea surface temperatures in the tropical Pacific and northern Arabian Sea, and internal atmospheric variability related to the circumglobal teleconnection pattern and the subtropical westerly jet stream, explain more than 70% of monthly summer precipitation variability in the 21st century. Several of these forcings have co-occurred with record strength during episodes of extreme monsoons, which have exacerbated the overall effect. Climate change may have contributed to increased variability and the in-phase co-occurrences of the identified mechanisms, but further research is required to confirm any such connection.

Introduction

Pakistan has experienced frequent extreme monsoon events in recent decades. At the turn of the century, Pakistan was exposed to one of the most severe droughts in its history (*1, 2*), while the floods of 2010 and 2022 were among the most devastating in modern times (*3, 4*). Considering West South Asia (WSA; 65°–75E° and 24°–37N°), the number of months with standardized precipitation anomalies exceeding ± 1 has increased by a factor of ˜1.4 between 1979–2000 and 2001–2022, while the number of months exceeding ± 1.5 has increased by a factor of 3.5 (Fig. 1). The large variations in the summer monsoon over WSA make a compelling case for climate change. However, despite the apparent increase in monsoon extremes, floods and droughts in this region predate modern climate change (*5, 6*). Therefore, it is essential to investigate these recent changes in the historical context to delineate the role of natural climate variability in driving such anomalies.

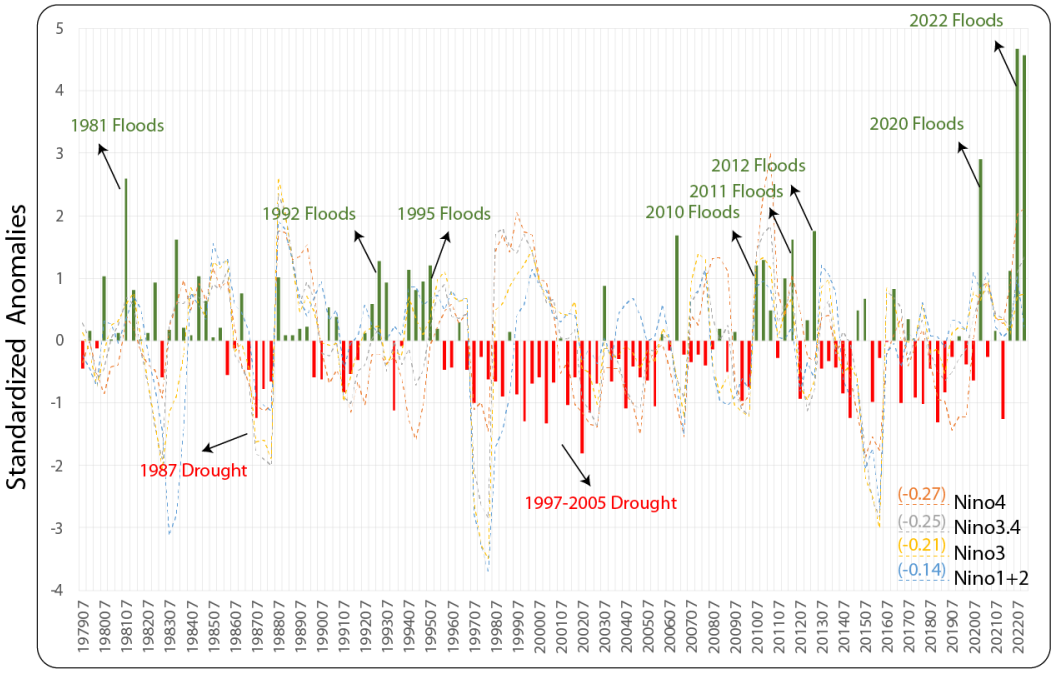

Figure 1: **July-August-September detrended CPC precipitation anomalies over West South Asia (WSA; 65–75°E; 24–37°N) during 1979–2022**. Monthly standardized area-averaged precipitation anomaly (bars) from the average over 1991–2020. The years when the region experienced floods or droughts are labeled. The dotted lines represent standardized Niño1+2 (blue), Niño3 (yellow), Niño3.4 (grey), and Niño4 (orange) indices using detrended COBE/NOAA sea surface temperatures. For ease of comparison, all Niño indexes are multiplied by -1 so that positive (negative) anomalies represent La Niña (El Niño). The number in parentheses represents the actual correlation between WSA and Niño indexes.

Although a substantially stronger (weaker) South Asian monsoon can significantly enhance (reduce) summer precipitation over WSA, the remarkably wet conditions experienced in the northwestern and southern Pakistan regions in recent years are extraordinarily unusual. These areas lie at the boundary of the South Asian monsoon and are usually beyond the reach of the most energetic weather systems capable of producing significant precipitation. The dry entrainment in the lower atmosphere, the strong westerlies in the

upper atmosphere over WSA (Fig. 2), and the low heat budget in the adjacent Arabian Sea make conditions unfavorable for rain-producing weather systems (*7*). Several factors – such as atmospheric wave activity triggered by distant teleconnections, circumglobal wave patterns, or jet stream anomalies – can overcome this unfavorable background environment and provide conditions conducive to above-normal monsoons (*8-11*). However, it is yet to be determined how much of a role these factors have played in recent extremes.

Many of Pakistan's extreme monsoons have happened during years with anomalous sea surface temperatures (SSTs) in the equatorial Pacific in connection with the phenomenon known as the El Niño–Southern Oscillation (ENSO). The most notable are droughts in 1997, 2002, and 2004 during El Niño (positive ENSO) and floods in 2010, 2011, and 2022 during La Niña (negative ENSO) (Fig. 1). Nevertheless, the monthly teleconnection of ENSO forcing on WSA summer precipitation is weak: not only is the severity of extreme monsoon conditions in Pakistan not proportional to the strength of ENSO forcing, but in several cases, the negative teleconnection even breaks downs. For instance, drought persisted in Pakistan even with extreme La Niña conditions during 1998–1999; likewise, despite strong El Niño, seasonal monsoon precipitation was average in 2015. This implies that other contributing factors, such as co-occurrences of other modes of variability, compensate for or compound the impact of ENSO.

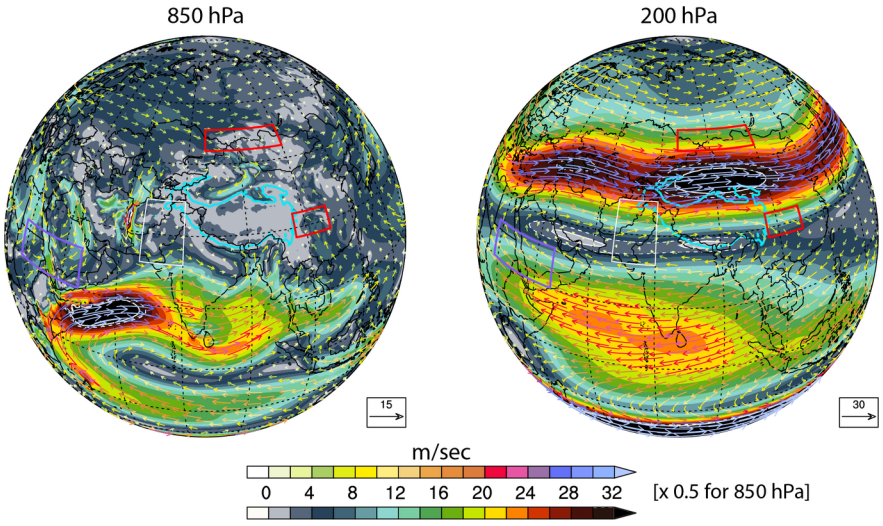

Figure 2: **The atmospheric circulation patterns during 1979–2022**. The upper (200 hPa) and lower (850 hPa) jet streams during the WSA summer monsoon season (July-August-September). The vectors (colors) represent the wind direction (speed). The rectangles indicate WSA (white) and areas used for two land surface temperature indexes. White contours identify South Asian high and jet stream maxima.

Evidence suggests that jet stream meandering in the Northern Hemisphere may be one of the contributors (*10-13*). On average, the subtropical westerly jet lies north of South Asia during the monsoon season (Fig. 2). In the summer of 2010, persistent extratropical upper-level blocking over western Russia led to the penetration of a deep trough over northern Pakistan through jet stream meandering (*10*). Western Russia suffered a record heatwave, and Pakistan experienced an unprecedented flooding event as a result. Likewise, in August 2022, the jet stream anomalies led to an upper-level atmospheric high over East Asia, created a frontal boundary over Pakistan, and pushed the South Asian monsoon trough south of its normal position. These conditions guided low-pressure monsoon systems westward and then meridionally through Pakistan along the frontal boundary (See animation in *Animation_1.mov*). The outcome was a record heatwave over East Asia (*14*) and catastrophic flooding over Pakistan. Apart from anomalies in the subtropical westerly

jet, the Circumglobal Teleconnection (CGT) pattern – the second leading mode of the upper atmosphere circulations in the Northern Hemisphere – has also been known to influence the precipitation distribution over WSA during summer (*15*), but its role in causing recent extreme monsoons is unclear.

Hosted file

`Animation_1.mov` available at https://authorea.com/users/532254/articles/630317-the-influence-of-natural-variability-on-extreme-monsoons-in-pakistan

***Animation Details**: The snapshot of atmospheric circulation (ERA5) and precipitation (CPC) over South Asia and the surrounding areas every three hours from August 10 to 26, 2022*

While ENSO forcing, jet stream meandering, and circumglobal wave activity are not new phenomena, the monsoon over Pakistan has become more erratic in recent years (Fig. 1). The recent extreme monsoon events have raised several questions. Is the increase in extreme monsoons over Pakistan due to natural variability alone, or has anthropogenic global warming played a role? If the former is true, has ENSO's influence on WSA precipitation increased in recent decades, or are other local or remote factors at play? Could these extremes result from the compounding effect caused by multiple forcings occurring simultaneously (e.g., remote teleconnections, jet stream anomalies, increased atmospheric water vapor, etc.)?

This study aims to investigate and answer these questions directly or indirectly. We hypothesize that internal atmospheric variability, such as anomalies in the jet stream and/or circumglobal wave activity, has contributed to unusual precipitation distributions over the WSA independent of well-known large-scale natural forcings. We examine this hypothesis using a regression model incorporating independent tropical and extratropical forcings capable of producing dynamical anomalies associated with extreme monsoons over the WSA.

Results and Discussion

Due to its location on the western edge of the South Asian monsoon, summer (July-September) precipitation in WSA is highly variable month-to-month, with a monthly standard deviation exceeding 70% of the seasonal average over most areas. The highest amounts of summer precipitation are experienced over Kashmir and northern Punjab in Pakistan (Fig. 3A). The strength of the monsoon is greatly diminished by the time it reaches eastern Afghanistan through the western border of Pakistan. However, monsoon magnitudes and variability have increased significantly in the peripheral regions of WSA over the past few decades. Notably, the mean and variability of precipitation along the Pakistan-Afghanistan border and Sindh province in southern Pakistan increased by over 100% between 1979–2000 and 2001–2022 (Fig. 3). The apparent increase in monsoon rains over these regions suggests a spatial shift in the location of wet anomalies maxima. An analysis of wet years with flooding since 1979 shows that in recent decades there have been more instances when excess precipitation has fallen in the northwestern and southern areas of WSA that historically received only trace amounts of monsoon precipitation (Fig. 4).

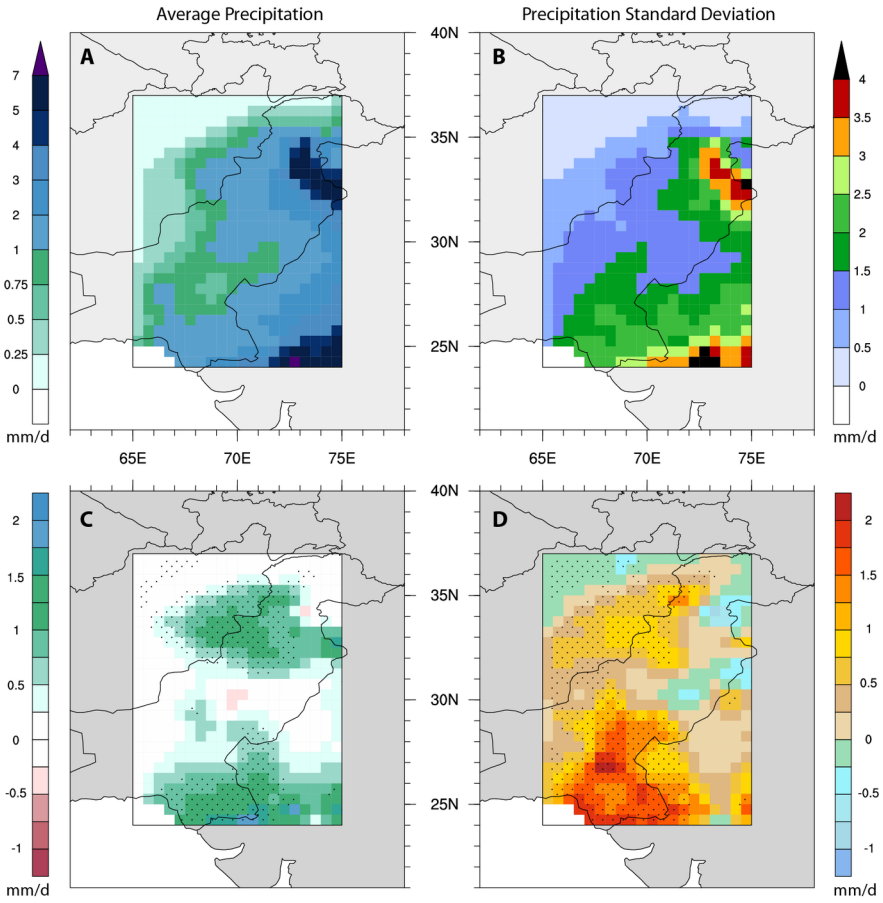

Figure 3: **July-August-September precipitation characteristics over WSA and its changes between 1979–2000 and 2001–2022**. Average (**A**) precipitation, (**B**) standard deviation in 1979–2022. The difference between average (**C**) precipitation and (**D**) standard deviation in 1979–2000 and 2001–2022. The stippling represents the statistical significance of differences at the 95% confidence level.

Identification of drivers

To understand the factors influencing changing precipitation patterns over WSA, it is imperative to determine what conditions allow monsoon weather systems to travel over peripheral regions where heavy monsoon rains do not normally penetrate. In addition to tropical forcings, our hypothesis that jet stream anomalies and/or circumglobal wave patterns can independently affect the monsoon distribution over WSA requires that we look beyond oceanic teleconnections. Jet stream anomalies and circumglobal wave activity often significantly affect land surface temperatures (*16-18*). Therefore, in addition to examining the relationship of WSA precipitation variability with natural variations in sea surface temperatures, we also examine connections between WSA precipitation variability and surface temperature anomalies over land. This will enable comprehensive identification of the modes of internal atmospheric variability that regulate anomalies in WSA precipitation.

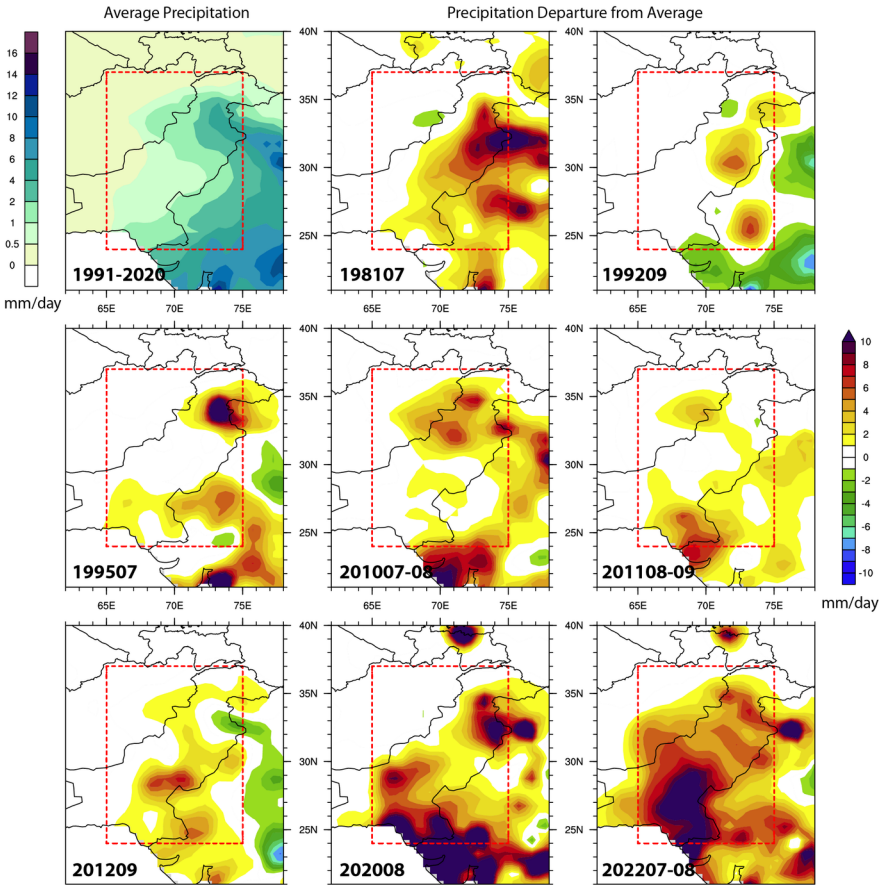

Figure 4: **Precipitation anomalies during Pakistan's flood years**. Average precipitation (top left) during the reference period (1991–2020). Precipitation departures from 1991–2020 average when Pakistan experienced floods. The months representing each event are provided in each panel.

An analysis of the spatial correlation map of detrended WSA precipitation and global surface temperatures reveals several oceanic and terrestrial regions of possible association. This includes SSTs in the tropical Pacific, north-central Pacific, and northern Arabian Sea, and land surface temperatures in East Asia, north-central Asia, Arabia, northeast Africa, and western Russia (Fig. 5A). These correlations may not be independent because large-scale climate forcings such as ENSO simultaneously affect many terrestrial regions through eastward propagating Rossby waves (*19*). Variability associated with ENSO in the tropical Pacific can also influence other oceanic basins through inter-basin interactions (*20*). As a result, many of these significant correlations between WSA precipitation and temperature over land and ocean regions may no longer exist once the influence of ENSO has been removed.

Therefore, we adopt a sequential procedure to construct a multi-linear regression model explaining WSA precipitation variability in which each additional explanatory variable is selected after eliminating the influence of the preceding explanatory variable from precipitation and surface temperatures. This process is repeated until all regions of interest have been identified. (See *Methods for complete details.*) Based on this approach, three oceanic and two land regions are identified as potential independent contributors to precipitation variability over WSA, including the east-central Pacific (i.e., the Niño3.4 region), West Pacific (WP), North Arabian Sea (NAS), East and north-central Asia, and Arabia/northeast Africa (Fig. 5B-5F).

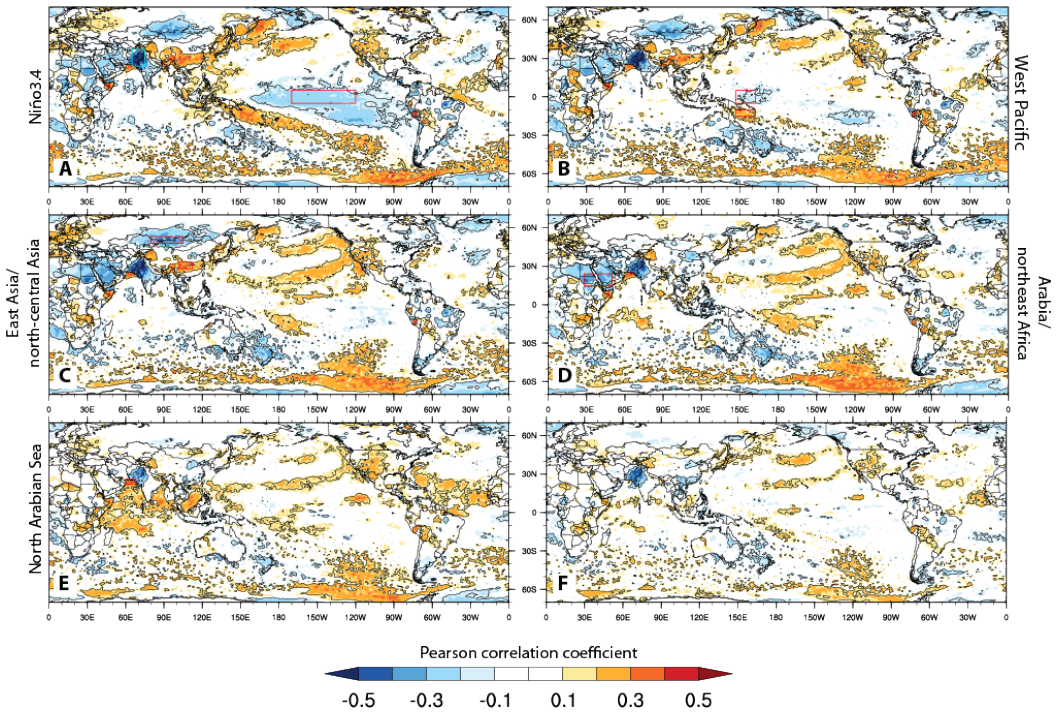

Figure 5: **Identification of relevant forcings affecting precipitation variability over WSA**. (**A**) Pearson correlation between monthly (July-August-September) WSA precipitation index (cyan rectangle box) and global surface temperatures. Same as (A), but after linearly removing the influence of (**B**) Niño3.4 temperature index from A, (**C**) West Pacific temperature index from B, (**D**) East and north-central Asia temperature index from C, (**E**) Arabia/northeast Africa temperature index from D. (**F**) represents the final correlation map after removing the influence of all five forcings. The red rectangle boxes and labels in (A) to (E) represent areas used to define each index. The black contours represent the statistical significance of correlations at the 90% confidence level.his is a caption

Given that the last two explanatory variables based on land surface temperatures (Fig. 3D, 3E) lack an obvious physical justification, we perform additional analyses to identify their robust connection with internal atmospheric variability. For this purpose, we calculate Empirical Orthogonal Functions (EOFs) using monthly 200 hPa geopotential height anomalies over an area encompassing 20°E–130°E and 20°N–65°N after linearly removing the influence of Niño3.4 and the WP SST variability. The subtropical westerly jet stream variability within this region is most relevant for the South Asian climate during the summer months. The resulting EOF patterns 1 through 6 are sufficiently separated from each other and explain >75% of the total variance (Fig. 6). However, we limit our focus to the first two EOFs that explain 21% and 17% of the total variance, respectively, and are the most related to the land-based temperature indexes and WSA precipitation variability.

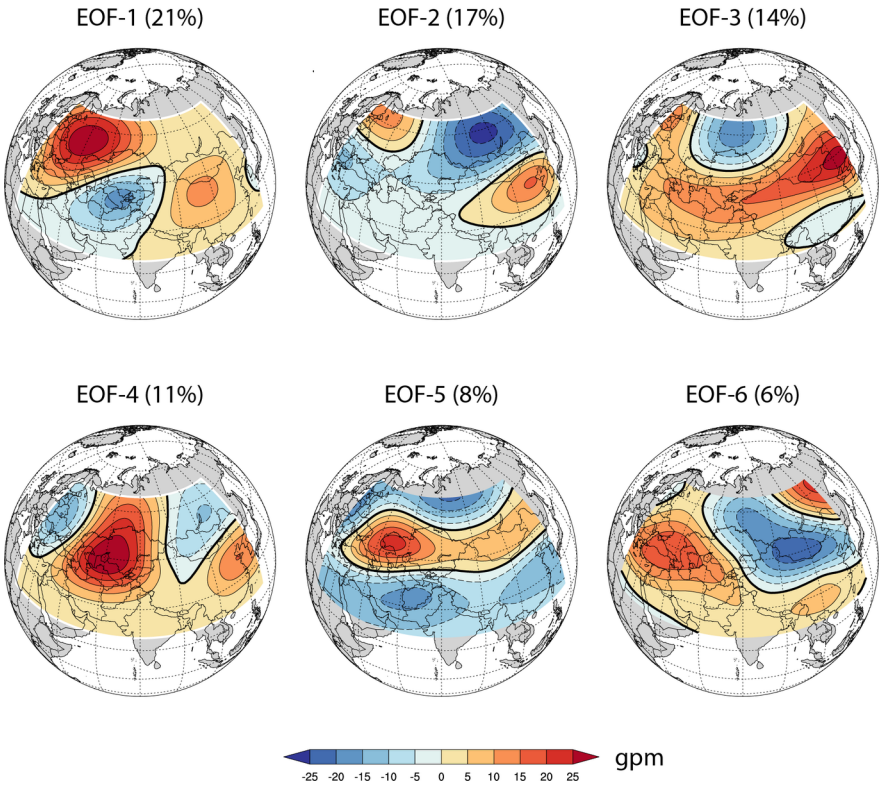

Figure 6: **Most common modes of the upper-atmosphere geopotential height variability**. The first six modes of EOF analyses of July-August-September 200 hPa geopotential height anomalies. The numbers in the parenthesis above each panel represent the explained variance. Each EOF pattern has been multiplied by the standard deviation of its principal component. All six EOF patterns are sufficiently separated based on the North's rule of thumb.

The spatial structure of the first EOF resembles the CGT pattern identified by Ding and Wang (*15*). It is possible to investigate this correspondence by regressing geopotential height anomalies onto the standardized index of CGT (see *Methods*) and the Principal Component (PC) time series of the first EOF. Regression maps derived from this analysis show a pattern correlation of 0.91 across the area used in EOF analyses and 0.69 across the Northern Hemisphere (Fig. 7). We also find a high temporal correlation (0.59) between the PC time series and the CGT index (Fig. 8), further supporting their close relationship. Therefore, we conclude that the first mode of 200 hPa geopotential height variability represents the CGT pattern.

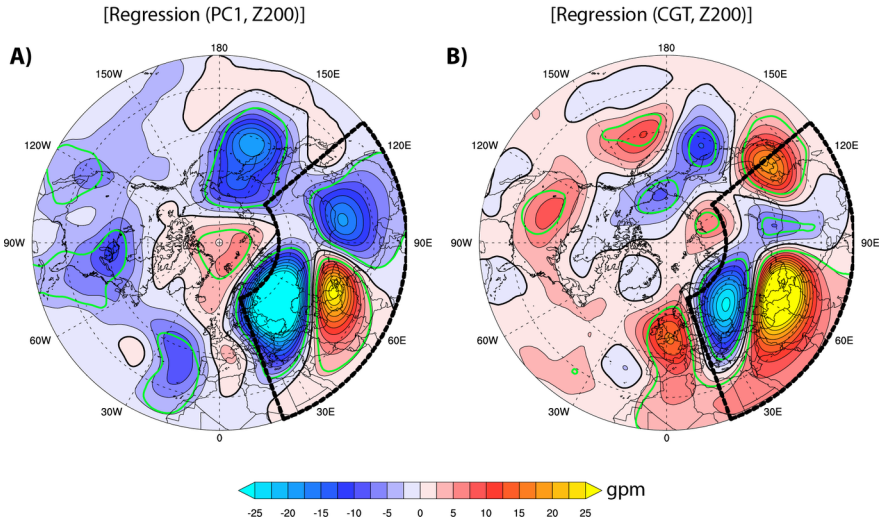

Figure 7: **Relationship between the leading mode of July-August-September geopotential height variability and CGT**. The 200 hPa monthly geopotential height (Z200) anomalies regressed onto the standardized (**A**) Principal Component associated with the first EOF (PC1) of Z200 and (**B**) CGT index. The black dotted box represents the area used to perform EOF analyses. The green contours represent statistically significant areas at the 95% confidence level. The analyses cover 1979–2022.

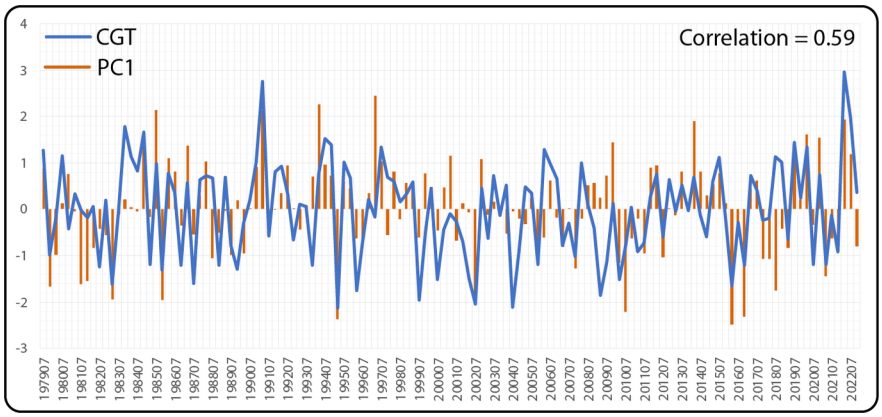

Figure 8: **Relationship between indexes**. CGT versus the principal component corresponding to the first EOF (PC1) of 200 hPa geopotential height variability.

Ding and Wang (*15*) also showed that the CGT pattern negatively correlates with temperature distributions in the Arabian Peninsula and the northeastern parts of Africa, which we have used to define one of our temperature indexes (Fig. 5D). In our analysis, this assertion holds only for the 21st century period when the temperature index over Arabia and northeast Africa significantly correlates with the CGT index (the correlation is -0.16 in 1979–2022 and -0.46 in 2001–2022; Fig. 9A). To discern the increasing influence of CGT on the pattern of temperature anomalies over Arabia and northeast Africa, we regress geopotential height anomalies onto the standardized temperature index (rectangle box shown in Fig. 5D) separately for the 1979–2000 and 2001–2022 periods (Fig. 10). When compared with the corresponding regression map based on the CGT index, the regression map for 2001–2022 (1979–2000) shows a pattern correlation of 0.91 (0.44) across the area used in EOF analyses and 0.63 (0.2) across the Northern Hemisphere. These

associations indicate that this temperature index is closely related to the CGT pattern in recent decades. Therefore, we refer to it as the temperature-based CGT index (TCGT).

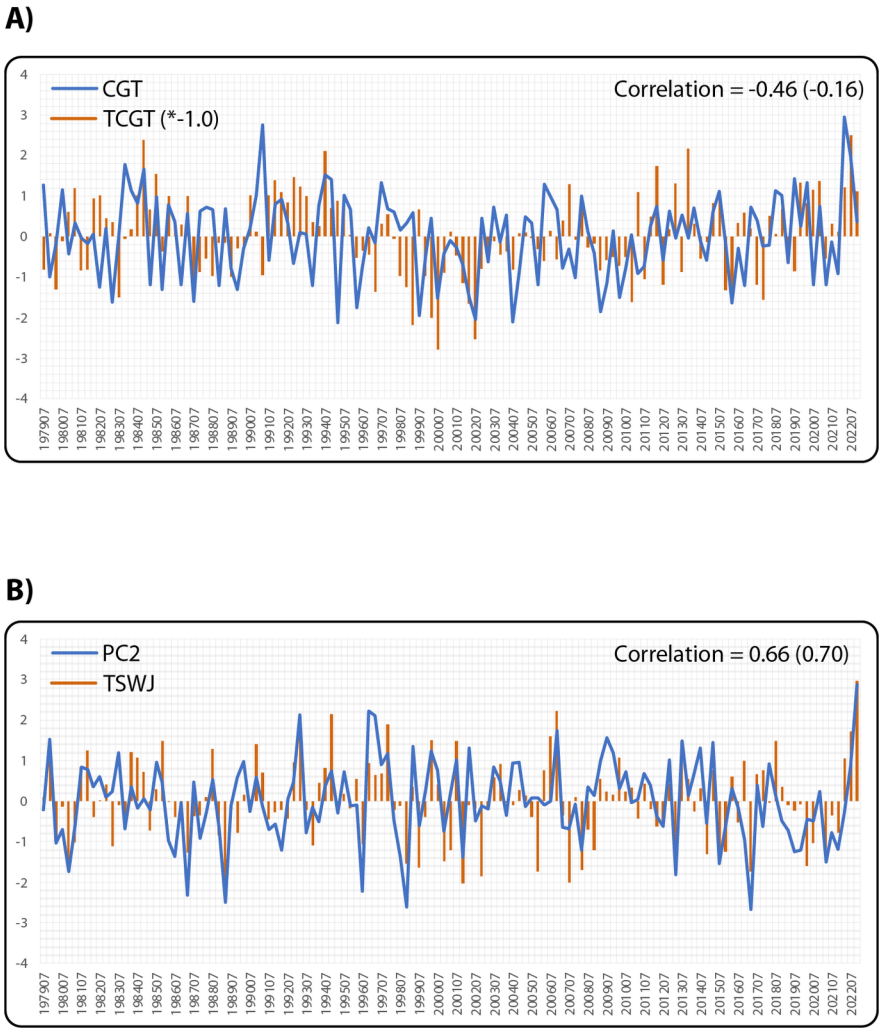

Figure 9: **Relationship between indexes**. (**A**) CGT versus TCGT, (**B**) the principal component corresponding to the second EOF (PC2) of 200 hPa geopotential height variability versus TSWJ. For ease of comparison, the TCGT time series is multiplied by -1. The numbers on each panel represent actual correlations during 2001–2022 (1979–2000).

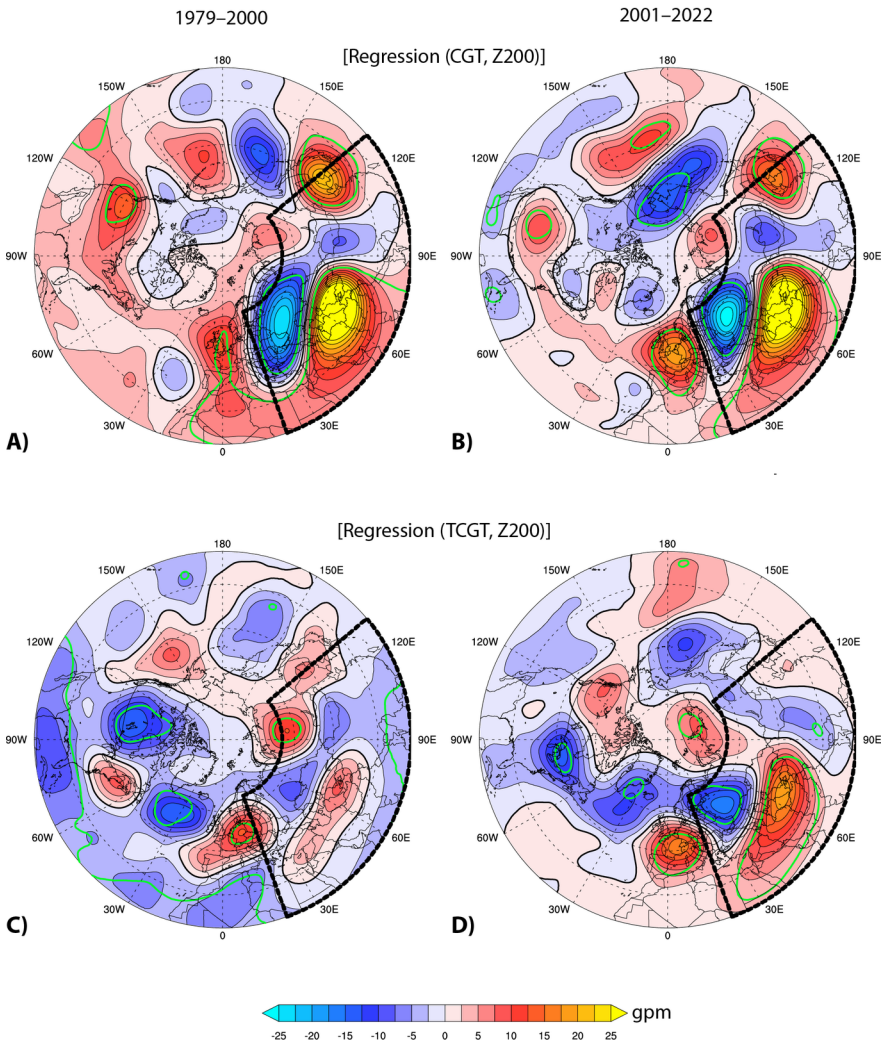

Figure 10: **Relationship between CGT and TCGT**. The 200 hPa monthly geopotential height (Z200) anomalies are regressed onto the standardized (**A**, **B**) CGT and (**C**, **D**) TCGT indexes. The TCGT is multiplied by -1 for ease of comparison. The black dotted box represents the area used to perform EOF analyses. The green contours represent statistically significant areas at the 95% confidence level. The analyses cover 1979–2000 (left column) and 2001–2022 (right column).

We note that the geopotential-based CGT index (*15*) significantly correlates with WSA precipitation, but the CGT correlation is not as strong as that of TCGT. Over the 1979–2022 period, the correlation of the CGT index with the WSA precipitation index is 0.27, while that of TCGT is -0.39. These significant correlations increase to 0.37 and -0.51 in recent decades (2001–2022). These comparisons suggest that the CGT pattern most affects the WSA precipitation distribution when it aligns in a way that affects the temperature distribution in the areas used to determine the TCGT.

The temperature dipole over East and north-central Asia (rectangle boxes shown in Fig. 5C) strongly relates to the second EOF of 200 hPa geopotential height (Fig. 6). We regress geopotential height anomalies onto the standardized Principal Component (PC) time series of the second EOF and this temperature index (Fig. 11). Comparing their regression maps reveals a pattern correlation of 0.95 across the area used in EOF analyses and 0.85 across the Northern Hemisphere. A robust temporal correlation (0.68) also exists between

the corresponding PC time series of the second EOF and the temperature index (Fig. 5C) for the entire analysis period (1979–2022) (Fig. 9B), which remains stable between the early (1979–2000; 0.7) and recent (2001–2022; 0.66) periods. These strong spatial and temporal correlations suggest that the temperature dipole over East and north-central Asia can be a proxy for the subtropical westerly jet variability (second EOF). Therefore, we call it the temperature-based subtropical westerly jet index (TSWJ). As in the case of the CGT index, the PC time series related to the second EOF correlates less strongly with the WSA precipitation index than the TSWJ index. Over the 1979–2022 period, the PC time series correlation with the WSA precipitation index is 0.27, while that of TSWJ is 0.41. This implies that when this mode of jet stream variability is aligned to have a maximum impact on temperature distribution in the two regions that define the TSWJ index, precipitation in WSA is most impacted by the meandering of the subtropical westerly jet stream.

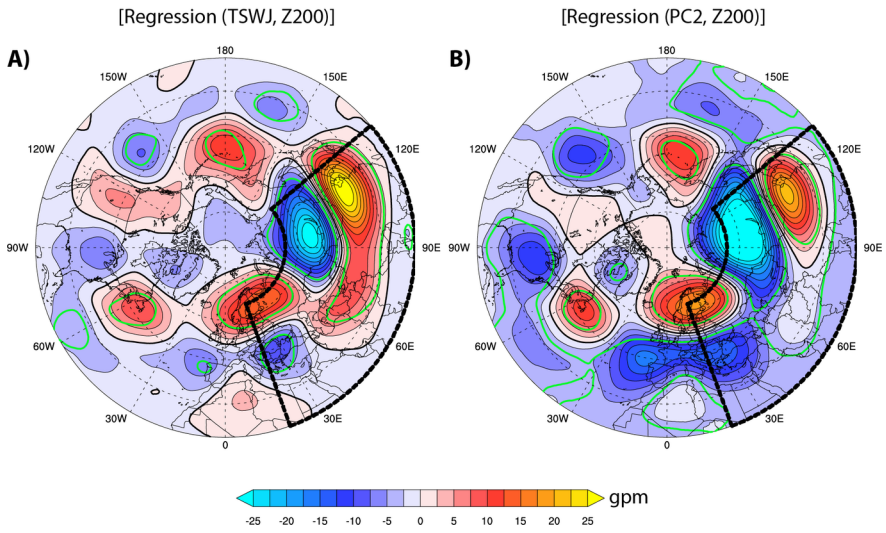

Figure 11: **Relationship between the second leading mode of July-August-September geopotential height variability and TSWJ**. The 200 hPa monthly geopotential height (Z200) anomalies regressed onto the standardized (**A**) TSWJ index and (**B**) Principal Component associated with the second EOF (PC2) of Z200. The black dotted box represents the area used to perform EOF analyses. The green contours represent statistically significant areas at the 95% confidence level. The analyses cover 1979–2022.

The influence of drivers

Knowing that the precipitation characteristics of WSA have changed significantly between the early (1979–2000) and recent (2001–2022) periods, we perform separate regression analyses for the two periods (after standardizing the data over the full 1979–2022 period). The regression model reveals a marked difference in explanatory power between the early and recent periods, as the coefficient of determination (R-squared) more than doubles across the entire region (Fig. 12A). Its maximum value remains below 0.35 for the early period, while it reaches 0.7 in many areas of Pakistan's southern half for the recent period.

The increase in explained variance over time has resulted from stronger correlations between WSA precipitation and all five independent forcings. For ease of comparison, the impact of each independent variable is expressed as the standardized precipitation anomaly (dependent variable) in response to per unit change in its standardized value (Fig. 12B-12F). The most notable shift in influence comes from the WP; while it provides little additional explanation of late-20th-century precipitation variability, it has been the most significant and widespread driver since 2000. The next major shift in influence is from TCGT, which displays a substantial increase in effect over the southern and eastern WSA. Other forcings also show an increase in

their impact on precipitation variability. ENSO (Niño 3.4) has a weak negative teleconnection over the east-northeast WSA in the early period, which becomes strong and spatially shifts westward over northwestern Pakistan – an area that has seen more frequent heavy precipitation events in recent years. The positive impact of warm SST anomalies in the northern Arabian Sea is predominantly felt in the southern WSA, which similarly gains strength, particularly along the coast. Likewise, the influence of TSWJ, represented by the East/north-central Asia temperature index, increases in strength and spatial footprint in the later period, substantially increasing over Balochistan and adjacent Afghanistan areas. Outside the WSA, these indexes also exhibit significant influence along the Western Ghats of southern India and central and northeastern South Asia.

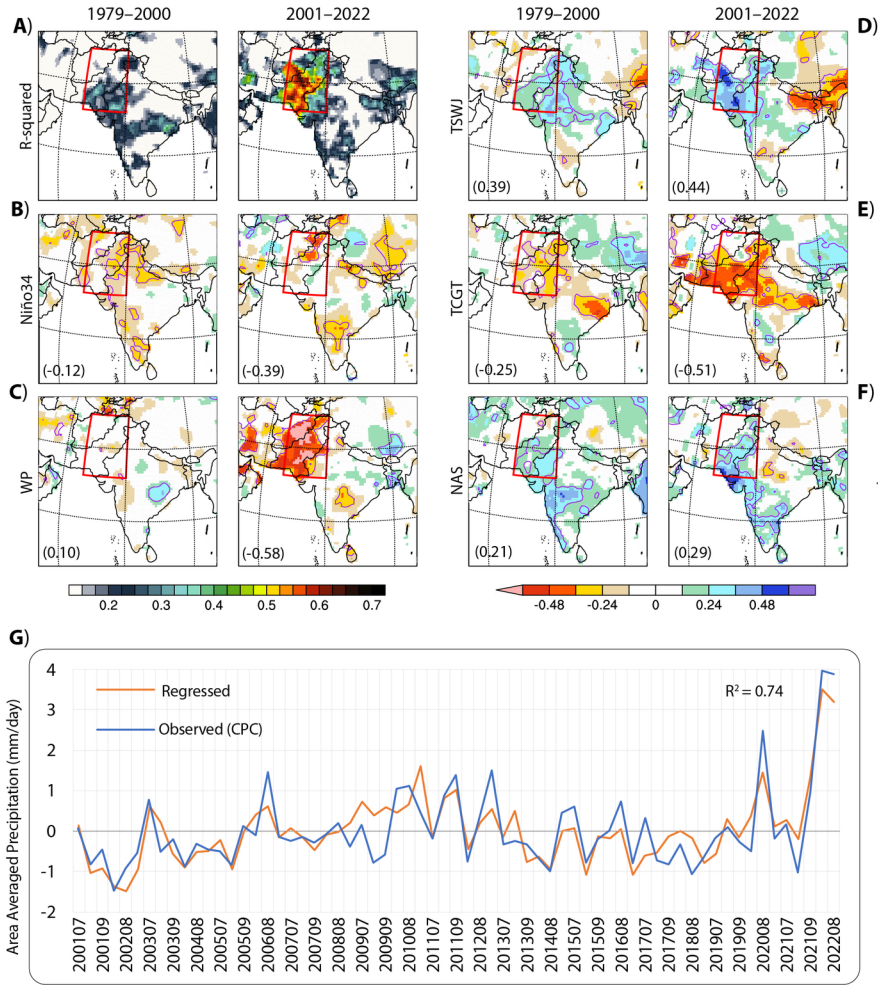

Figure 12: **Multiple linear regression analyses of monthly WSA precipitation. (A) The coefficient of determination (R2)**. The standardized regression coefficients describe each explanatory variable's influence on WSA precipitation, including (**B**) Niño3.4, (**C**) WP, (**D**) TSWJ, (**E**) TCGT, and (**F**) NAS. The first and third columns represent 1979–2000, and the second and fourth columns represent 2001–2022. The purple contours show statistically significant areas at 95% confidence levels. The numbers in each panel represent the correlation between the time series of each explanatory variable and the WSA precipitation index. (**G**) The actual and regressed monthly (July-August-September) anomalies from 2001 through 2022.

Given the increased precipitation variability, a high number of wet and dry extremes, and the substantial explanatory power of the regression model in the recent period, we mostly focus on the 21st-century period in the rest of the analyses. The regression based on standardized data over the length of the recent period displays high skill in calculating monthly precipitation variability (R^2= 0.74). There has only been one notable exception in the sign of the precipitation anomaly since 2000, when the model failed to capture below-normal monsoon rains in 2009 (Fig. 12G), highlighting the potential role of other factors not considered in the regression. The explanatory power of the regression model for the recent period does not substantially change (R^2= 0.71) when regression is performed over the entire period (Fig. 13).

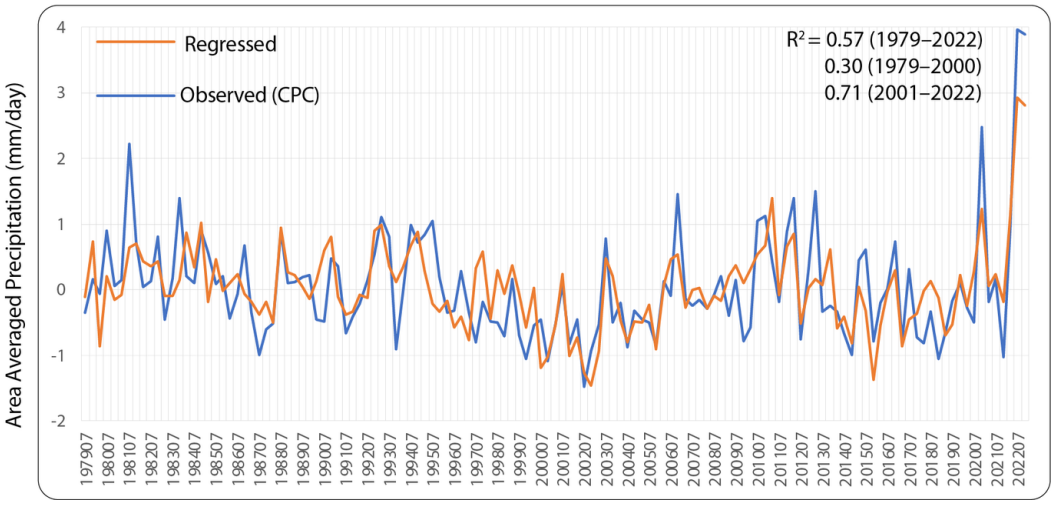

Figure 13: **Multiple linear regression analyses of WSA precipitation over 1979–2000**. The actual and regressed monthly (July-August-September) anomalies during 1979 and 2022.

To understand how each of the five forcings influences the variability of WSA precipitation in the recent period, we repeat multiple linear regression analyses using geopotential height as the dependent variable instead of precipitation for the 2001–2022 period. A separate analysis is conducted for geopotential height fields at 850 and 200 hPa. An individual regression coefficient represents geopotential anomalies in geopotential meters per unit change in the standardized explanatory variable (Fig. 14). However, before analyzing the dynamic anomalies caused by these forcing factors, it is imperative to understand why the vigor of rain-producing systems decreases as they approach the peripheral monsoon regions of the WSA. Once we know the climatological atmospheric conditions over the WSA, it should be easier to comprehend how atmospheric anomalies caused by individual forcings shape associated anomalies in precipitation distributions.

In the lower atmosphere over the Arabian Sea, before the northern flank of the Somali jet comes onshore, its moist flow mixes with the dry air entraining from the northwest. A narrow passageway formed by the Hindukush mountains to the east and the Lut desert to the west channels this dry air from central Asia (Fig. 2). The dry entrainment keeps southwest parts of South Asia under conditions less favorable for moist convection (*21*). As a result, the monsoon trough forms along the Himalayas between the Bay of Bengal and northwestern South Asia rather than having an east-west orientation. These areas also sit on the western edge of the South Asian High in the upper atmosphere as the southern flank of the subtropical westerly jet runs diagonally through the WSA (Fig. 2). Consequently, low-pressure monsoon systems moving along the monsoon trough cannot penetrate further west (*22*). Other factors, such as interaction with the topography and the depletion of moisture supply far inland, also favor the dissipation of these systems by the time they reach Kashmir and Punjab in Pakistan. As a result, southern, southwestern, and western South Asia remain relatively dry.

The climatological conditions over WSA (Fig. 2) highlight several prerequisites that must be met before the monsoon can penetrate the southern and western parts of the region. These factors include reduced dry entrainment from the northwest into the Somali jet over the Arabian Sea and weakened onshore flow over southern WSA, allowing the possibility of an east-west orientation of the monsoon trough. Additionally, a more favorable placement of the subtropical westerly jet should allow monsoon rain-producing systems to penetrate the west-northwest regions of WSA. With this knowledge of the preconditions, we now analyze the regression coefficients associated with the forcings used in the regression model.

The coefficients corresponding to Niño3.4 represent atmospheric anomalies induced by La Niña. They show an anomalous easterly flow from the Bay of Bengal through central India to southern parts of WSA (Fig. 14A). This reflects a reduction in dry air entrainment over the northern Arabian Sea and southern WSA. In the upper atmosphere, an anomalous high to the northeast and a low to the northwest create a frontal boundary over northwestern Pakistan that should help facilitate the movement of low-pressure systems through that area. The tropical easterly jet also shows strengthening over the western Indian Ocean and the Arabian Sea. It also supports an anomalous barotropic high over western Russia, which, combined with the low to the northwest of Pakistan, partly resembles atmospheric anomalies during July-August 2010. Anomalously low Niño3.4 values during this period indicate the occurrence of an unusually strong La Niña for this time of year.

Lower-level circulation anomalies induced by Niño3.4 and WP forcings are peculiarly similar from East Asia to the southwestern boundary of WSA through the Bay of Bengal and central India (Fig. 14B). However, the WP influence differs from Niño3.4 in other areas. In addition to reducing dry air entrainment over WSA, the WP weakens the Somali jet over the Arabian Sea and southwesterly flow over the Bay of Bengal by inducing anomalous westward flow from the western Pacific/eastern Indian Ocean. The resulting changes in monsoon circulation weaken the monsoon over Bangladesh and northeast India and redistribute moist flow over western South Asia. In the upper atmosphere, the WP forcing places a quasi-diagonally elongated low-pressure anomaly between northern Egypt and to the west of northwest Pakistan and a high-pressure anomaly over East Europe. These conditions represent a weakening of westerly flow over the northern WSA that should allow monsoon lows to penetrate further west. Furthermore, the placement of the anomalous low along the western Pakistan border guides the movement of monsoon lows meridionally through Pakistan. The corresponding precipitation regression maps show that these dynamical anomalies bring excess monsoon rains throughout the region. The warming in the northern Arabian Sea leads to an anomalous cyclonic circulation over the Arabian Sea, with the center off the coasts of the states of Gujarat and Maharashtra in western India (Fig. 14C). The excess moisture convergence, as a result, increases rainfall, particularly along the coastal belt in these Indian states and Sindh in Pakistan, as well as upstream regions in central Pakistan.

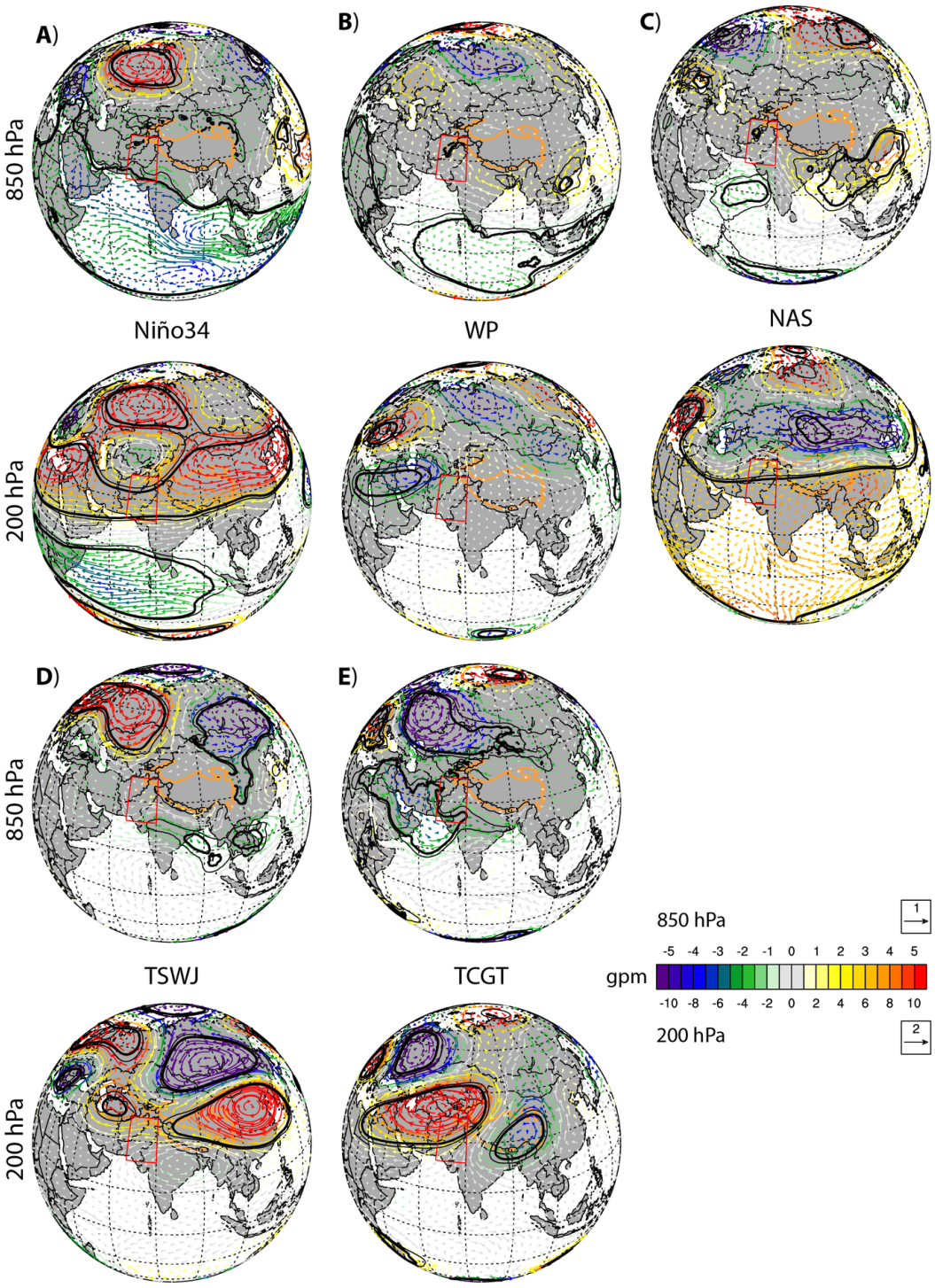

Figure 14: **Multiple linear regression analyses of atmospheric circulation anomalies**. The regression coefficients describe atmospheric anomaly patterns (850 hPa and 200 hPa) associated with each standardized explanatory variable in the regression model. (**A**) Niño3.4, (**B**) WP, (**C**) NAS (**D**) TSWJ, (**E**) TCGT. The vectors represent atmospheric winds, and the colors represent geopotential height. The thick and thin black contours represent the statistical significance of geopotential height regression coefficients at 95% and 90% confidence levels, respectively. The analyses cover 1979–2022. For ease of comparison, we multiply coefficients corresponding to Niño34, WP, and TCGT by -1 so that all coefficients reflect those phases of forcings that induce positive precipitation anomalies over WSA.

As previously shown, TCGT represents the CGT pattern, and TSWJ is a proxy for the second EOF of 200 hPa geopotential height variability. In response to TSWJ forcing, the subtropical westerly jet is forced northward over East Asia, which creates an anomalous barotropic shear over South Asia and places the monsoon trough south of its original position over southern WSA (Fig. 14D). TCGT also causes a similar increase in barotropic shear in the lower atmosphere and a southward movement of the monsoon trough over South Asia (Fig. 14E). Anomalies with such characteristics facilitate the westward trajectory of Bay of Bengal monsoon lows towards southern Pakistan and produce conditions conducive to the genesis of monsoon vortices (See animation in *Animation_2.mov*). TSWJ induces much stronger dry entrainment from eastern Asia over northeastern South Asia, and consequently, the negative precipitation response is greater than that of TCGT. In contrast, the moisture convergence along the monsoon trough, caused by increased westerly flow from the northern Indian Ocean, is stronger under TCGT than under TSWJ, which significantly influences precipitation over Central India. Both forcings lead to a high-pressure anomaly in northwest WSA, reflecting a northwest shift in the westerlies in the upper atmosphere. Such conditions facilitate the movement of rain-producing weather systems over the southern-southwestern WSA, but keep them out of the northwestern WSA. As a result, these forcings have a limited role in causing excess precipitation over the northwestern WSA in wet months.

Hosted file

`Animation_2.mov` available at https://authorea.com/users/532254/articles/630317-the-influence-of-natural-variability-on-extreme-monsoons-in-pakistan

***Animation Details**: Isosurface of specific humidity (0.0123 Kg/Kg) colored by zonal winds. The strongest colors represent magnitudes greater than ± 10 m/sec. Warm (cold) colors indicate eastward (westward) flow. The animation runs from July 01 to August 31, 2022. The convergence zone generally represents the position of the monsoon trough. The data used in this animation is obtained from ERA5 reanalysis. The animation shows a snapshot every three hours.*

Robustness of identified forcings

A critical question is whether combining these five forcings can accurately reproduce atmospheric anomalies associated with precipitation variability over South Asia and its surrounding regions. The answer to this question should allow us to determine whether these forcings are robust drivers of precipitation variability over WSA in recent decades. We seek answers to this question in two ways. First, we perform a composite analysis of precipitation distribution and overlying circulation patterns during wet and dry months over WSA. Even though the regression model only explains the precipitation variance over WSA, we assume the WSA anomalies cannot be completely disassociated from the average large-scale pattern of precipitation anomalies across South Asia. Therefore, we compare precipitation composites over the entire South Asia in this analysis. There have been stronger wet extremes than dry extremes over WSA during the last 22 years. Using a 1.0 standard deviation threshold, we identify eight extreme wet months and four extreme dry months; using a 0.75 standard deviation threshold increases the number of wet and dry months to 11 and 13, respectively. Note that the area-averaged monthly precipitation distribution in WSA is highly skewed and does not contain ˜32% of the total events within one standard deviation (which would be expected in a normal distribution). Therefore, we use the 0.75 standard deviation threshold for composite analyses. Second, we analyze individual monthly cases to understand the dynamical patterns associated with WSA precipitation extremes and their reproducibility through the regression model. In this case, we consider those 12 months where below-normal or above-normal WSA precipitation departures exceed one standard deviation. The precipitation anomalies in these individual cases are only shown over WSA.

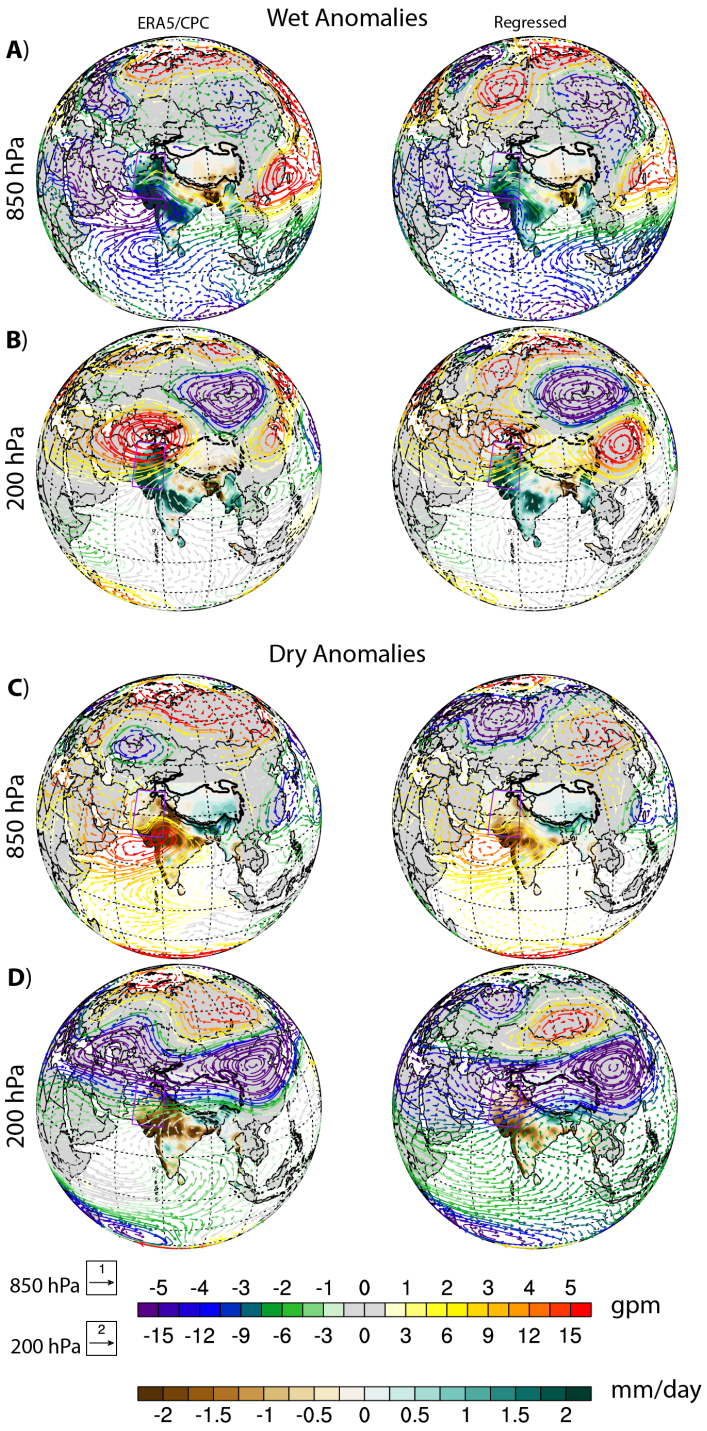

Figure 15: **Composite analyses of atmospheric circulation and precipitation anomalies in 2001–2022**. The composites of wet (**A**, **B**) and dry (**C**, **D**) precipitation anomalies in South Asia and associated atmospheric (850 and 200 hPa) anomalies. The left column represents actual precipitation (circulation) anomalies in CPC (ERA5), and the right column represents corresponding anomalies in the regressed data. The vectors represent atmospheric winds, and the colors represent geopotential height. The wet and dry anomalies are defined using a 0.75 standard deviation threshold of the WSA precipitation index.

Anomalously wet months feature a southward-shifted monsoon trough, a cyclonic anomaly over the northern Arabian Sea, and a substantially weakened entrainment of dry northerly flow over the Arabian Sea and southern WSA in the lower atmosphere (Fig. 15A). The dipolar anomaly in the north and east of South Asia in the upper atmosphere, resembling the TSWJ-induced pattern, highlights the importance of subtropical westerly jet stream meandering in shaping conditions conducive to wetter-than-normal monsoon rains over WSA. Additionally, an upper atmosphere high, partly resembling the TCGT-induced pattern, is needed over northwest WSA to displace westerlies so that monsoon lows can penetrate further west over South Asia (Fig. 15B). The anomalies over higher latitudes and East Asia are barotropic in nature. The regressed patterns represent all these key features of atmospheric anomalies supporting wet conditions over WSA. Interestingly, the correspondence of broad precipitation anomalies between actual and regressed patterns is not limited to WSA. The suppression over Bangladesh and northeastern India, and enhancement over Myanmar, central India, and the Western Ghats, compare remarkably well between the actual and regressed patterns, indicating that these forcing mechanisms explain precipitation anomalies across South Asia.

The magnitude of precipitation suppression during drier-than-normal months is not comparable to wet extremes during wetter-than-normal months over WSA (Fig. 15C). This asymmetry is to be expected, as the dry anomalies cannot exceed the climatological precipitation amounts a region receives. Therefore, the strongest dry anomalies would always occur in areas that, on average, receive the highest rainfall during the monsoon season. As a result, while the maximum wet anomalies occur over the peripheral monsoon regions of WSA, the maximum dry anomalies occur over the eastern parts of WSA that climatologically experience more monsoon rains. Apart from this artifact, the broad pattern of anomalies in precipitation distribution during below-average months is the opposite of that observed in above-average months, with less rain falling in the Western Ghats and central India and excessive rain falling in northern India.

While atmospheric anomalies during the dry months composite are not an exact reversal of those during the wet months composite, some features are comparable. The anticyclonic anomaly over the Arabian Sea, the reversal of jet stream-related anomalies over East Asia and Siberia, and the northward shift in the monsoon trough are a few features that are opposite to the anomalies during wet months (Fig. 15C, 15D). Additionally, the westerly jet moves further south over western Asia, preventing rain-producing weather systems from having trajectories through WSA. A substantial weakening of tropical easterlies over the Indian Ocean is also present during dry extremes. The strength of the tropical easterly jet stream is normally associated with the strength of the South Asian summer monsoon (*23*). Therefore, their weakening reflects that the South Asian monsoon is likely weaker-than-normal when below-normal monsoon rains are received over WSA. Stronger-than-normal tropical easterly jet activity is not clear in the wet months composite.

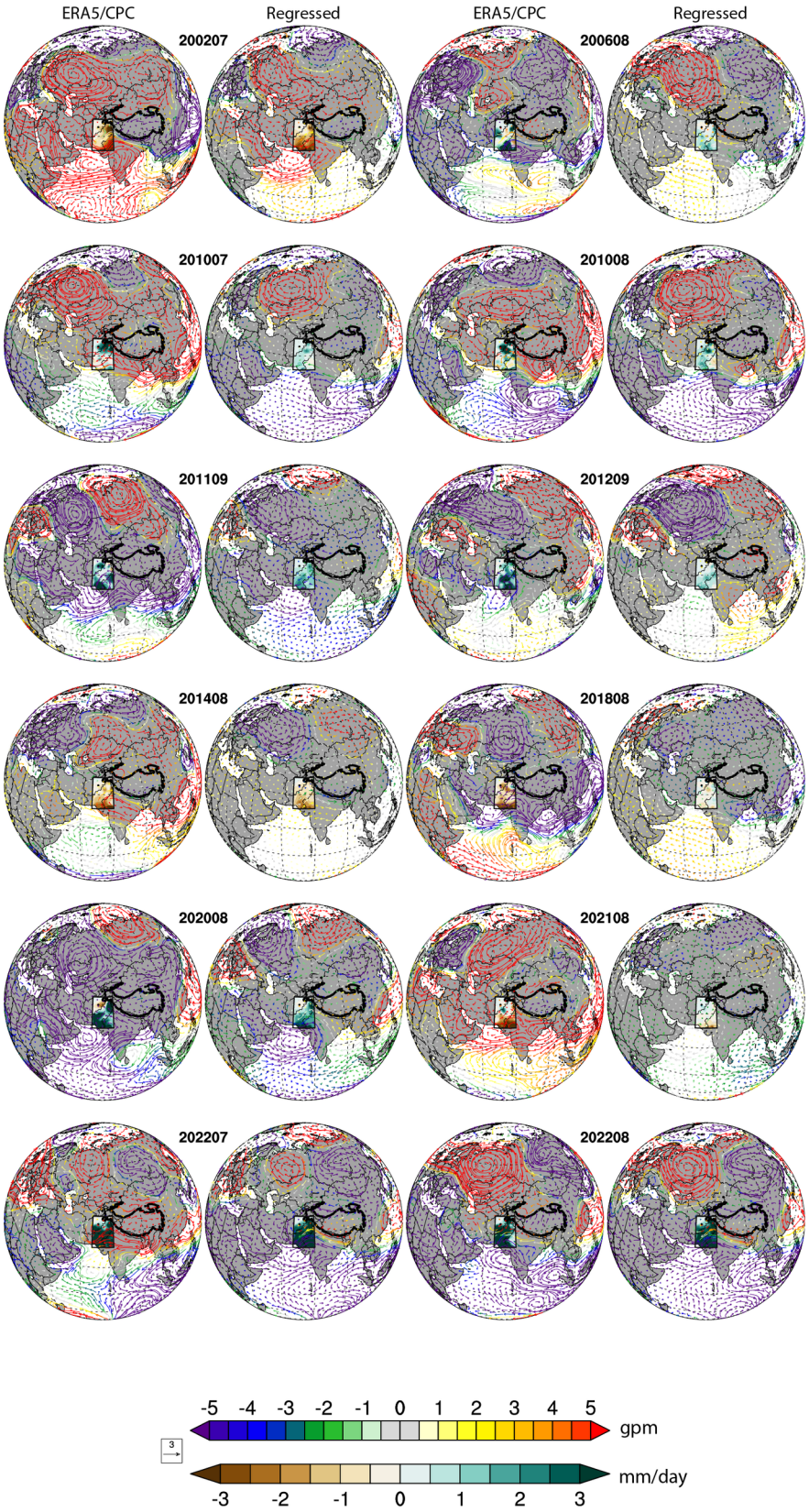

Figure 16: **Analyses of atmospheric circulation and precipitation anomalies in extreme months**. The wet and dry precipitation anomalies over WSA and associated atmospheric anomalies at 850hPa. The first and third columns represent actual precipitation (circulation) anomalies in CPC (ERA5), and the second and fourth columns represent corresponding anomalies in the regressed data. The vectors represent atmospheric winds, and the colors represent geopotential height. The wet and dry anomalies are defined using a 1.0 standard deviation threshold of the WSA precipitation index. The analyses cover 2001–2022.

The regression-based anomalies are mostly comparable to the actual patterns in those months when precipitation amounts exceed one standard deviation, with the most notable differences being in August 2018 and 2021 (Figs. 16 and 17). The two most common features across all these extreme months are lower atmosphere cyclonic (anticyclonic) anomalies over the Arabian Sea and southward (northward) shifts in the monsoon trough in wet (dry) months. The wet anomalies over the southern WSA most commonly require anomalous high pressure over the northwestern WSA and a jet stream pattern normally induced by positive TSWJ forcing over East Asia in the upper atmosphere. The wet anomalies over northwestern WSA mostly require an overlying trough in the upper atmosphere. Nevertheless, the dynamical anomalies in dry or wet months display a substantial variety in patterns causing those extremes, highlighting the complexity of interactions that shape the distribution of monsoon extremes over WSA.

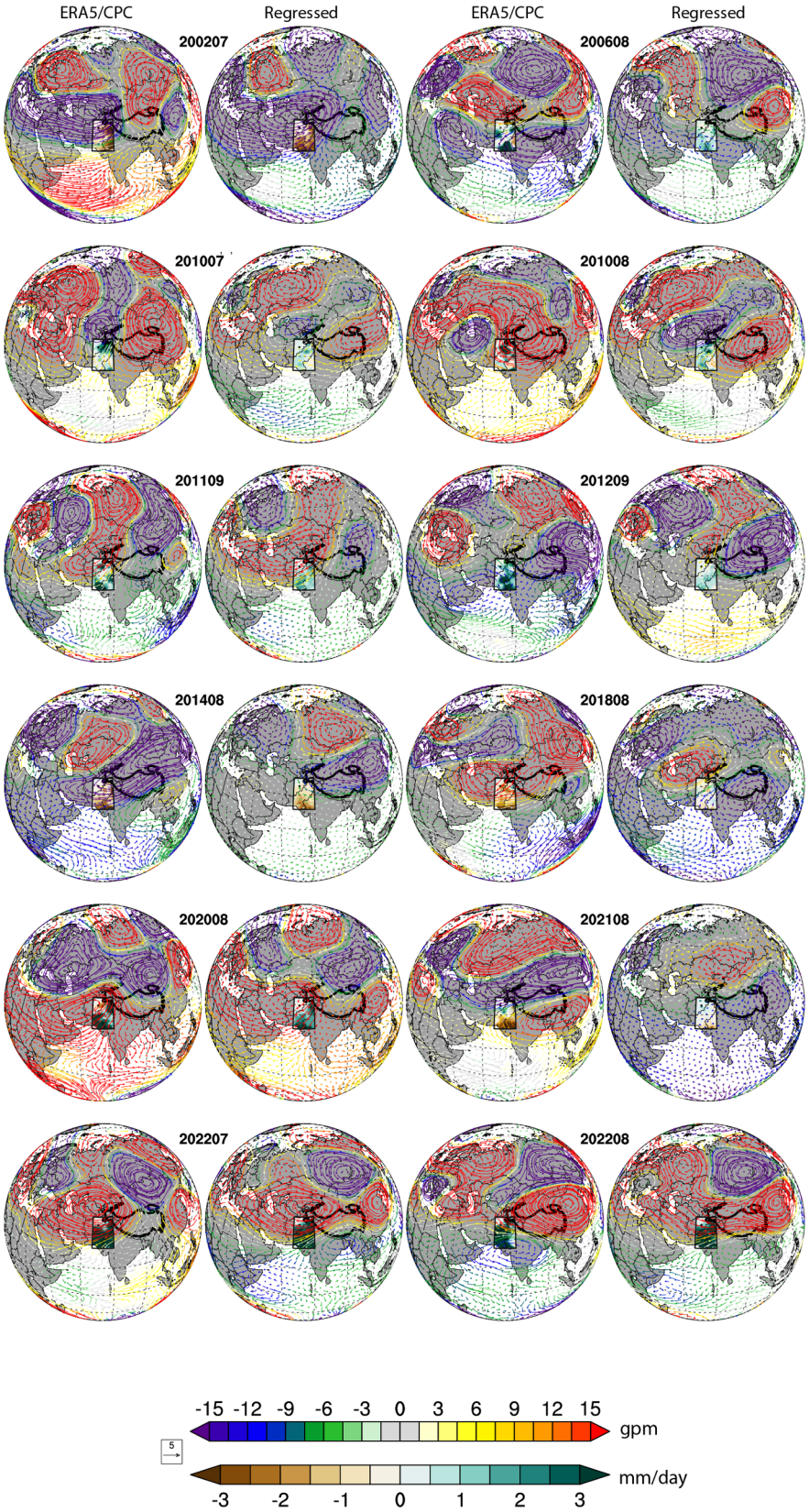

Figure 17: Same as in Figure 16 but with circulation anomalies at 200 hPa.

Co-occurring non-ENSO factors

According to our analysis, internal atmospheric variability and other oceanic forcings have contributed to unusual precipitation distributions over the WSA independent of conventionally defined ENSO (i.e., by the Niño3.4 index). In addition, we can provide answers to the questions that motivated this study. It is not only the negative ENSO teleconnection that has strengthened and shifted spatially in the 21st century, contributing to excessive rainfall in Pakistan's northwest and neighboring areas in Afghanistan; two other oceanic forcings also have a role in precipitation variability over the WSA. A dipole of SSTs between the equatorial western Pacific and northeast of the Australian coast (WP index; rectangle boxes in Fig. 5B) provides additional Pacific Ocean influence on WSA precipitation variability independent of ENSO. There is a need for additional empirical and model-based research to understand the true nature of WP forcing. Nevertheless, it does not appear to be a remnant of SST variability in the equatorial central Pacific. The Northern Hemisphere atmospheric wave response to WP forcing differs substantially from the response to Niño3.4 (Fig. 18). A second oceanic forcing can be attributed to anomalies in the adjacent Arabian Sea (NAS index; rectangle box in Fig. 5E). Although conditions in the northern Arabian Sea primarily determine the NAS forcing, it generally represents variability in SSTs across the tropics, independent of Niño3.4 and WP (Fig. 5E, 5F). Also, the CGT pattern and the meandering of the subtropical westerly jet have played an instrumental role in facilitating the dynamic forces necessary to guide monsoon lows over the peripheral regions of the WSA.

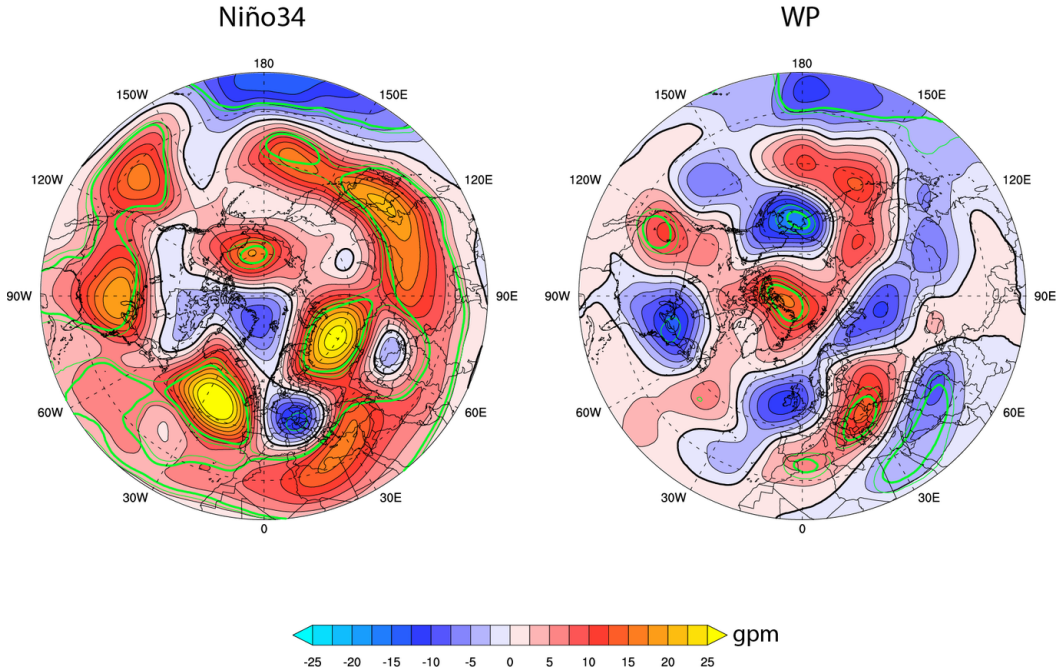

Figure 18: Comparison of atmospheric wave response in the Northern Hemisphere produced by Niño34 and WP forcings. The regression coefficients describe atmospheric anomaly patterns associated with standardized Niño3.4 (left) and WP (right) forcings. The colors represent geopotential height anomalies. The thick and thin green contours represent the statistical significance of regression coefficients at 95% and 90% confidence levels, respectively. The analyses cover 2001–2022.

Moreover, there is evidence that more synchronous occurrences of these forcings have shaped the unusual and unprecedented distribution of monsoon rains over WSA over the past few decades. This conclusion can be demonstrated by a simple transformation of the monthly time series representing five forcings. First, we

multiply the standardized indexes associated with Niño3.4, WP, and TCGT with -1 so that positive values in each index should positively correlate with WSA precipitation variability and vice versa. Second, we assign a -1 (+1) value to monthly indexes crossing -1 (+1) and replace the rest of the time series with zeros. Lastly, we sum each month across the five indexes. The resulting time series displays an increase in the simultaneous occurrence of those phases of the five forcings that compound each other's impact. For example, during 1979–2000, there were ten instances when net in-phase forcings were two or more, compared with sixteen cases during 2001–2022. Furthermore, from 1979 to 2022, six times the net in-phase forcings were three or more, with all but one occurring between 2001 and 2022 (Fig. 19).

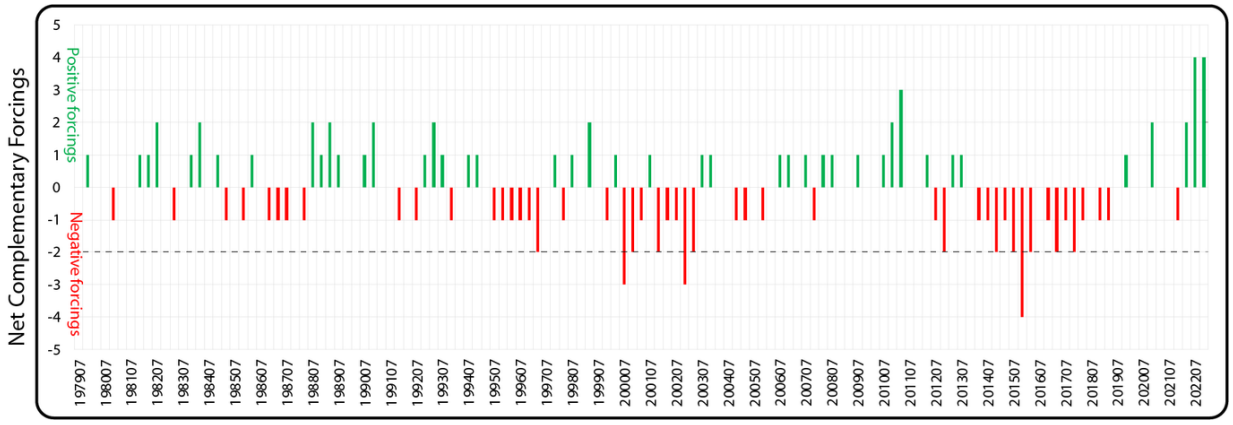

Figure 19: **Net complimentary forcings**. The sum of all forcings after their standardized monthly indexes are transformed into +1/-1 or 0 using ±1 standard deviation as a threshold. The resulting +ve (-ve) number represents the net forcings at the monthly scale that positively (negatively) influence WSA precipitation. Niño3.4, WP, and NAS forcings are multiplied by -1, so positive values in each index positively correlate with WSA precipitation.

There has also been a significant change in the variability of some of these forcings in the 21st century. With a 30% increase in variability, WP exhibits the greatest change in the recent period. The standardized WP forcings were strongest in July 2022 (-4.0), August 2022 (-3.3), and August 2010 (2.9) (Fig. S20). These were the three months during which Pakistan experienced flooding. The standardized TSWJ in August 2022 (3.0) and TCGT in July 2022 (-2.4) were also the highest and second strongest during 1979-2022. TSWJ exhibits a 10% increase in variability, while TCGT displays a slight decrease of -5%. The other forcings, Niño3.4 and NAS, show reduced variability in 2001–2022, with 18% and 15% declines compared to 1979–2000. How these decreases might have impacted their influences on WSA precipitation is unclear.

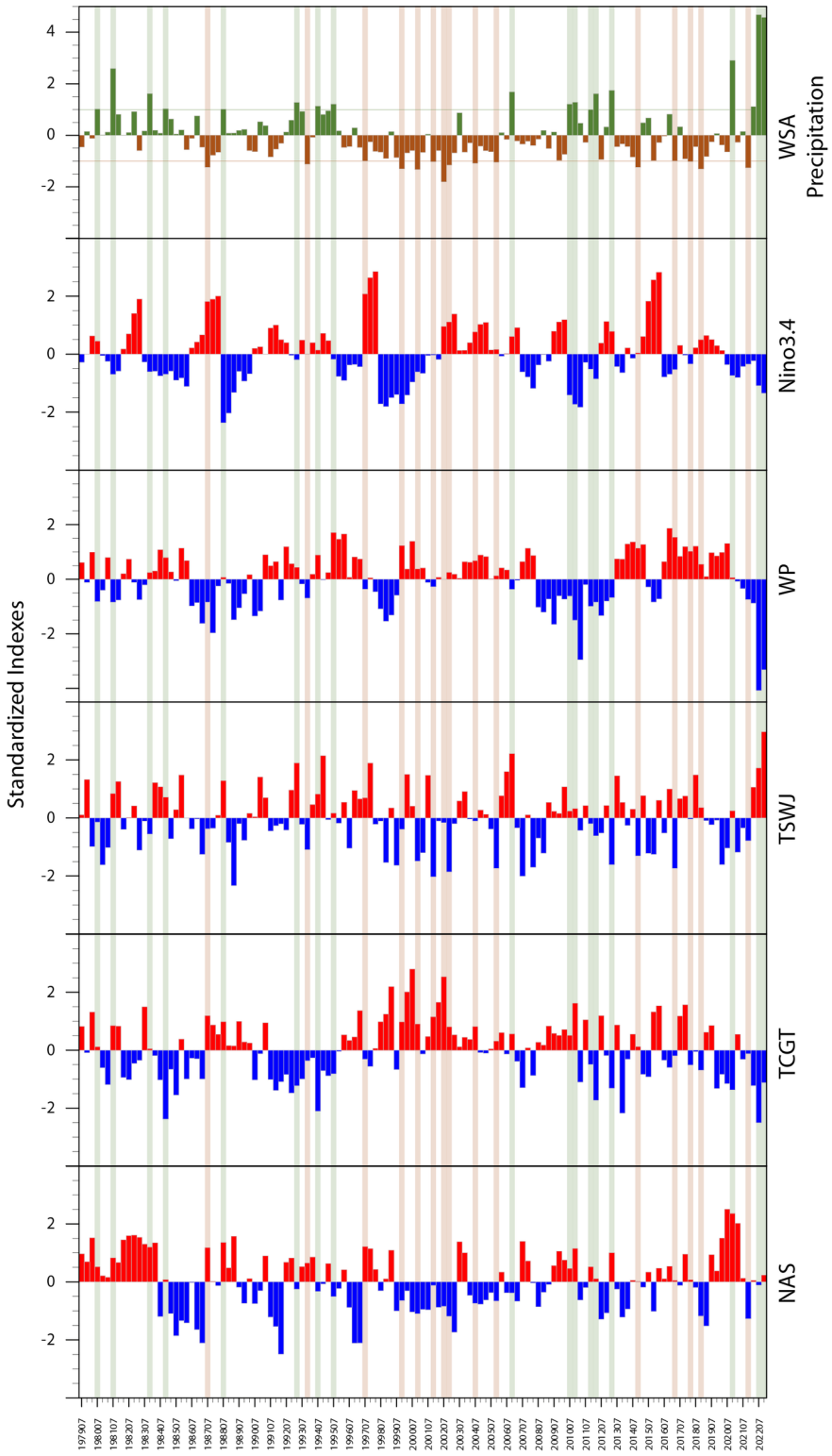

Figure 20: The standardized indexes of WSA precipitation and five forcings. The shaded brown/green months represent precipitation anomalies over WSA exceeding ±1 standard deviation.

Implications and outlook

Our study shows that natural variability in oceanic and atmospheric processes is responsible for the increased variability in precipitation over the WSA in recent decades. The monsoon over South Asia is one of the most extensively researched topics in climate science. However, monsoon precipitation variability over WSA is relatively poorly understood. Since most of the WSA lies at the periphery of the South Asian monsoon, heavy rains rarely penetrate the region, and precipitation variability (relative to precipitation mean) is significantly higher than in other parts of South Asia. Thus, it has unique prerequisites for extreme monsoons that involve the simultaneous occurrence of multiple naturally occurring modes of oceanic and atmospheric variability, creating an environment where weather systems can move over the western periphery of the South Asian monsoon. We have shown that the number of naturally occurring WSA-relevant modes in these synchronous occurrences has increased in recent decades and that several of these forcings have occurred with record strength. These factors have led to substantially more variability in precipitation and unprecedented rains over WSA in the 21st century.

Despite our ability to replicate atmospheric patterns and anomalies in precipitation distribution associated with wet and dry extremes over WSA through multiple linear regression, several knowledge gaps remain that will require further investigation. For example, a deeper understanding of SST dipole-based WP forcing is required. Moreover, while we have clarified why we preferred land-based temperature indexes as explanatory variables over PC time series and CGT index, additional research is necessary to identify more robust indexes that could serve as predictors representing relevant modes of atmospheric variability that influence WSA precipitation.

Additionally, we do not reject the possibility of climate change contributing to increased precipitation variability in the WSA. Among the consequences of climate change are record-high temperatures on land, such as those recorded in Russia in 2010 and East Asia in 2022. Although the atmospheric patterns that have caused these particular heatwaves have been attributed to natural oceanic and atmospheric variability (*24, 25*), climate change may have a role in intensifying these dynamic anomalies. There is also evidence that climate change has caused more compound extremes over the past few decades (*26, 27*). The increased in-phase co-occurrence of factors affecting WSA precipitation variability may also be related to climate change, though that connection has not yet been established. Moreover, we do not exclude the possibility of thermodynamic influences, such as increased atmospheric water vapor, that can enhance precipitation intensity when these in-phase co-occurrences occur. We have analyzed linear associations between understudied sources of natural variability and WSA precipitation variability, probably proximate forcings of extremes in a changing climate, but it cannot be ruled out that nonlinear forces could play a role, which must be investigated separately.

Taken together, our results clearly identify modes of variability as a critical influence on recent extreme events in the region and also highlight the need for further research to systematically and robustly identify a clear link between climate change and extreme monsoons in the WSA.

Materials and Methods

Datasets

The analyses presented in this study are based on global land precipitation, land and ocean surface temperatures, atmospheric geopotential height, meridional winds, zonal winds, and specific humidity. From 1979 to 2022, it covers the months of July, August, and September, except for September 2022. Global land precipitation and maximum and minimum temperatures are sourced from the Climate Prediction Center (CPC), with a horizontal grid spacing of 0.5° by 0.5°. The mean land temperature is calculated by averaging the maximum and minimum temperatures. Global sea surface temperature (SST) data come from two sources. The Centennial in situ Observation-Based Estimates (COBE; (*28*)) SST, available at 1.0° by 1.0°, covers 1979 to 1981, and the NOAA high-resolution analysis of SST, available at 0.25° by 0.25°, covers

1982 to 2022. The National Oceanic and Atmospheric Administration (NOAA) Physical Science Laboratory, Boulder, Colorado, USA (https://psl.noaa.gov) provides all global land precipitation and land and ocean surface temperature datasets. The remaining atmospheric variables are retrieved from the European Centre for Medium-Range Weather Forecasts Reanalysis 5 (ERA5), available at 0.25° x 0.25° horizontal grid spacing (*29*). We combine multiple SST sources to ensure the highest resolution data is used for the investigation. The SSTs and atmospheric variables are remapped to the CPC data grid (0.5° by 0.5°) using the bilinear interpolation function implemented in the Climate Data Operators (CDO; https://code.mpimet.mpg.de).

Methods

We focus on the West South Asia (WSA) region from 65°–75E° and 24°–37N°, which encompasses most of Pakistan, western parts of India, and eastern parts of Afghanistan. In South Asia, the monsoon season lasts from June to September. However, the WSA region receives monsoon precipitation between July and September; all monsoon-related extremes over this region have occurred during these months. Therefore, all analyses are based on this July-to-September monsoon season.

We remove the monthly least square linear trend at each grid point from all datasets for analyses. Anomalies are calculated using 1991–2010 as the reference period. To develop a regression model for WSA monsoon precipitation, we identify possible explanatory variables based on the global land and ocean temperature correlations with the WSA precipitation index. Our method involves selecting surface temperature-based independent explanatory variables sequentially, where each previous explanatory variable's influence is removed linearly before the next is identified. We start with a Pearson correlation map of the WSA precipitation index and global surface temperatures over 1979–2000. Many oceanic and land regions show significant association with WSA precipitation, including SSTs in the equatorial Pacific, North Pacific, and northern Arabian Sea, and land surface temperatures in East Asia, north-central Asia, Arabia, northeast Africa, and western Russia (Fig. 5A).

As ENSO is the most robust natural forcing, we begin by selecting the Niño3.4 index (shortened to Niño3.4 in the text), which is the area-averaged SST anomaly from 190–240°E and -5–5°N, as our first explanatory variable. Niño3.4 SSTs display a negative association with WSA precipitation, consistent with the general understanding that ENSO exhibits a negative teleconnection with the South Asian summer monsoon. Removing the Niño3.4 influence from precipitation and temperature eliminates tropical Pacific correlation except for an area in the western Pacific exhibiting a meridional correlation dipole (Fig. 5B). We select this dipole as the second explanatory variable for the regression model, defined as the temperature difference in the rectangle area spanning 147°E–162°E and 5°S–5°N from that spanning 147°E–162°E and 15°S–10°S. WSA precipitation's correlation with western Russia temperatures diminishes once the tropical Pacific influence is removed, but several other correlations remain intact, including a significant positive correlation with surface temperatures over East Asia and a significant negative correlation with surface temperatures over north-central Asia bordering Mongolia and Siberia. Due to their location, we assume these temperature anomalies are likely related and reflect the meandering of the subtropical westerly jet stream (Fig. 2). Therefore, the third explanatory variable is based on the temperature difference between the area covering 102–112°E and 28–33°N and the area covering 80–105°E and 48–53°N (Fig. 5C). The fourth explanatory variable in our regression model is the temperature over Arabia and northeast Africa. This area negatively correlates with the CGT pattern (*15, 30*) (Fig. 9) and therefore represents the influence of one of the dominant modes of internal atmospheric variability in the Northern Hemisphere. We defined it as the temperature over the region covering 28–50°E and 15–24°N (Fig 5D). The fifth and final explanatory variable uses SSTs in the North Arabian Sea between 60–68°E and 20–26°N, which have a strong positive relationship with WSA precipitation variability (Fig 5E). The importance of each of the five selected explanatory variables is determined by comparing the R^2 and F-test statistics (Fig. 21).

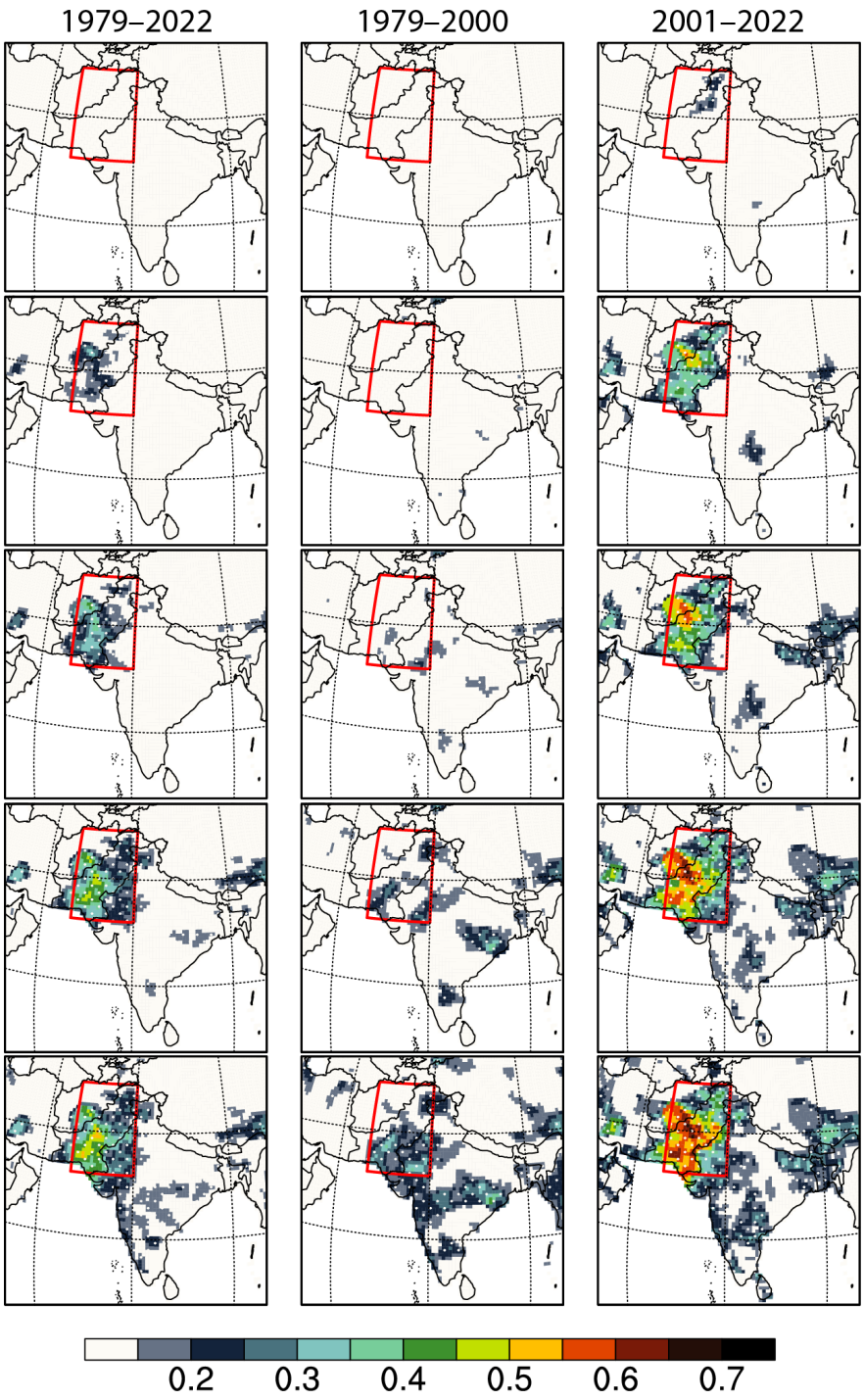

Figure 21: **The importance of each explanatory variable in multiple linear regression analyses of monthly (July-August-September) precipitation**. Precipitation variability explained by the (multi; row 2–5) linear regression model, expressed as the coefficient of determination (R2), with each explanatory variable added. Stippling represents the 95% confidence level for F-statistics significance. The analyses are shown for the full (1979–2022; left column), early (1979–2000; middle column), and recent (2001–2022; right column) periods. The red rectangular box represents West South Asia.

After removing the influence of these indexes, no major areas of significant correlation exist between WSA precipitation and global surface temperature except for an area in the northern Pacific (Fig 5F). Using this region as an additional explanatory variable in the regression does not add much to the explained variance, and therefore this region is not considered for analyses. The rectangle boxes for the explanatory variable 2 to 5 represent those areas that yield maximum correlation with the WSA precipitation index after area averaging. All area averages are performed after weighting the data with the cosine of latitudes.

We determined a statistically significant difference in precipitation mean and variability between early (1979–2000) and recent (2001–2022) periods across WSA (Fig. 2) through Student's t-test and F-test, respectively. Therefore, we use the five explanatory variables to investigate the drivers of these precipitation differences by performing separate multiple regression analyses for the early and recent periods. Similar analyses are conducted for the entire period (1979–2022). Additionally, we perform multiple regression analyses separately for geopotential height, zonal winds, and meridional winds as dependent variables.

All regression analyses that compare early and recent periods or cover the entire length of the analysis period employ standardized data based on 1979–2022. The regression analyses focused on the recent 21st-century period use standardized data covering only that period. All regression results are tested for statistical significance using analysis of variance.

To further aid the analyses, the CGT index is defined as geopotential height area weighted averaged over 35°–40°N, 60°–70°E, following Ding and Wang (*15*). Similarly, Niño4, Niño3, and Niño1+2 indexes are defined using the climate data guide provided by the National Center for Atmospheric Research (https://climatedataguide.ucar.edu/climate-data).

References

1. H. Xie, C. Ringler, T. J. Zhu, A. Waqas, Droughts in Pakistan: a spatiotemporal variability analysis using the Standardized Precipitation Index. *Water Int* **38**, 620-631 (2013).

2. S. Adnan, K. Ullah, S. T. Gao, Investigations into Precipitation and Drought Climatologies in South Central Asia with Special Focus on Pakistan over the Period 1951-2010. *J Climate* **29**, 6019-6035 (2016).

3. S. Mallapaty, S. Soofi, Z. Memon, Pakistan's floods have displaced 32 million people - here's how researchers are helping. *Nature* **609**, 667-667 (2022).

4. K. Gaurav, R. Sinha, P. K. Panda, The Indus flood of 2010 in Pakistan: a perspective analysis using remote sensing data. *Nat Hazards* **59**, 1815-1826 (2011).

5. B. Weil, The Rivers Come: Colonial Flood Control and Knowledge Systems in the Indus Basin, 1840s–1930s. *Environment and History* **12**, 27 (2006).

6. S. Dutt, A. K. Gupta, B. Wunnemann, D. D. Yan, A long arid interlude in the Indian summer monsoon during similar to 4,350 to 3, 450 cal. yr BP contemporaneous to displacement of the Indus valley civilization. *Quatern Int* **482**, 83-92 (2018).

7. S. S. C. Shenoi, D. Shankar, S. R. Shetye, Differences in heat budgets of the near-surface Arabian Sea and Bay of Bengal: Implications for the summer monsoon. *J Geophys Res-Oceans* **107**, (2002).

8. S. Saeed, W. A. Muller, S. Hagemann, D. Jacob, Circumglobal wave train and the summer monsoon over northwestern India and Pakistan: the explicit role of the surface heat low. *Clim Dynam* **37**, 1045-1060 (2011).

9. F. S. Syed, J. H. Yoo, H. Kornich, F. Kucharski, Extratropical influences on the inter-annual variability of South-Asian monsoon. *Clim Dynam* **38**, 1661-1674 (2012).

10. W. K. M. Lau, K. M. Kim, The 2010 Pakistan Flood and Russian Heat Wave: Teleconnection of Hydrometeorological Extremes. *J Hydrometeorol* **13**, 392-403 (2012).

11. G. Di Capua *et al.*, Drivers behind the summer 2010 wave train leading to Russian heatwave and Pakistan flooding. *Npj Clim Atmos Sci* **4**, (2021).

12. A. Bibi, K. Ullah, Y. S. Zhou, Z. Q. Wang, G. T. Shouting, Role of Westerly Jet in Torrential Rainfall During Monsoon Over Northern Pakistan. *Earth Space Sci* **7**, (2020).

13. A. Schneidereit *et al.*, Large-Scale Flow and the Long-Lasting Blocking High over Russia: Summer 2010. *Mon Weather Rev* **140**, 2967-2981 (2012).

14. Z. Q. Wang, H. L. Luo, S. Yang, Different mechanisms for the extremely hot central-eastern China in July-August 2022 from a Eurasian large-scale circulation perspective. *Environ Res Lett* **18**, (2023).

15. Q. H. Ding, B. Wang, Circumglobal teleconnection in the Northern Hemisphere summer. *J Climate* **18**, 3483-3505 (2005).

16. X. L. Chen, T. J. Zhou, Relative contributions of external SST forcing and internal atmospheric variability to July-August heat waves over the Yangtze River valley. *Clim Dynam* **51**, 4403-4419 (2018).

17. J. Q. Yang *et al.*, Atmospheric Circumglobal Teleconnection Triggered by Spring Land Thermal Anomalies over West Asia and Its Possible Impacts on Early Summer Climate over Northern China. *J Climate* **34**, 5999-6021 (2021).

18. W. W. Wang, W. Zhou, X. Wang, S. K. Fong, K. C. Leong, Summer high temperature extremes in Southeast China associated with the East Asian jet stream and circumglobal teleconnection. *J Geophys Res-Atmos* **118**, 8306-8319 (2013).

19. K. E. Trenberth *et al.*, Progress during TOGA in understanding and modeling global teleconnections associated with tropical sea surface temperatures. *J Geophys Res-Oceans* **103**, 14291-14324 (1998).

20. W. J. Cai *et al.*, Pantropical climate interactions. *Science* **363**, 944-+ (2019).

21. W. R. Boos, J. V. Hurley, Thermodynamic Bias in the Multimodel Mean Boreal Summer Monsoon. *J Climate* **26**, 2279-2287 (2013).

22. D. Rastogi *et al.*, Characteristics of Bay of Bengal Monsoon Depressions in the 21st Century. *Geophys Res Lett* **45**, 6637-6645 (2018).

23. D. R. Pattanaik, V. Satyan, Fluctuations of Tropical Easterly Jet during contrasting monsoons over India: A GCM study. *Meteorol Atmos Phys* **75**, 51-60 (2000).

24. R. Dole *et al.*, Was there a basis for anticipating the 2010 Russian heat wave? *Geophys Res Lett* **38**, (2011).

25. D. Q. Zhang, L. J. Chen, Y. Yuan, J. Q. Zuo, Z. J. Ke, Why was the heat wave in the Yangtze River valley abnormally intensified in late summer 2022? *Environ Res Lett* **18**, (2023).

26. M. R. Alizadeh *et al.*, A century of observations reveals increasing likelihood of continental-scale compound dry-hot extremes. *Sci Adv* **6**, (2020).

27. J. Wang *et al.*, Anthropogenically-driven increases in the risks of summertime compound hot extremes. *Nat Commun* **11**, (2020).

28. S. Hirahara, M. Ishii, Y. Fukuda, Centennial-Scale Sea Surface Temperature Analysis and Its Uncertainty. *J Climate* **27**, 57-75 (2014).

29. H. Hersbach *et al.*, The ERA5 global reanalysis. *Q J Roy Meteor Soc* **146**, 1999-2049 (2020).

30. M. Almazroui, I. U. Rashid, S. Saeed, M. N. Islam, ENSO influence on summer temperature over Arabian Peninsula: role of mid-latitude circulation. *Clim Dynam* **53**, 5047-5062 (2019).

Acknowledgments

This research used the Oak Ridge Leadership Computing Facility resources, a DOE Office of Science User Facility supported under Contract DE-AC05-00OR22725.

Funding:

This work is supported by the U.S. Air Force Numerical Weather Modeling Program and National Climate-Computing Research Center, located within the National Center for Computational Sciences at the ORNL, and supported under a Strategic Partnership Project 2316-T849-08 between DOE and NOAA.

Author contributions:

M.A. designed the study and performed the analyses. All authors were involved in the discussion of results. M.A. wrote the manuscript draft and finalized it with feedback from all authors.

Competing interests:

The authors declare that they have no competing interests.

Data and materials availability:

All datasets used in this analysis are publicly available. The Centennial in situ Observation-Based Estimates SST, the NOAA high-resolution analysis of SST, and the CPC precipitation and temperature data are provided by the NOAA PSL, Boulder, Colorado, USA, from their website at https://psl.noaa.gov. The ERA5 reanalysis is available from the Copernicus Climate Change Service (C3S) Climate Date Store (https://cds.climate.copernicus.eu/).